Origin of the Wangpingxigou Pb-Zn deposit in East Qinling orogenic belt, China: Distal response to the giant Donggou porphyry Mo system?

Chang Jin[a,b], Wei Terry Chen[a], Xin-Yu Gao[b], Xiao-Chun Li[c], Zhi-Wei Bao[b], Tai-Ping Zhao[b,*]

[a] State Key Laboratory of Ore Deposit Geochemistry, Institute of Geochemistry, Chinese Academy of Sciences, Guiyang 550081, China
[b] Key Laboratory of Mineralogy and Metallogeny, Guangzhou Institute of Geochemistry, Chinese Academy of Sciences, Guangzhou 510640, China
[c] Department of Earth Sciences, The University of Hong Kong, Pokfulam Road, Hong Kong, China

A B S T R A C T

The southern margin of the North China Craton (NCC) hosts many world-class porphyry Mo and vein-type Pb-Zn $\pm$ Ag deposits, forming an important polymetallic metallogenic belt in China, even over the world. Although the Mo and Pb-Zn $\pm$ Ag mineralization are temporally and spatially associated with each other, their possible genetic links are still unclear. To delineate the relationships between the two types of ore mineralization, we carried out *in-situ* geochemical and S-Pb isotopic analyses on sulfides from the two spatially associated deposits, i.e., the Wangpingxigou Pb-Zn and Donggou porphyry Mo deposits in the ore district.

Based on field and microscopic observations on the crosscutting relationships of various veins and paragenetic relationships of various hydrothermal minerals, three (I–III) and four (I–IV) stages of hydrothermal veins have been identified in the Wangpingxigou and Donggou deposits, respectively. Pyrite grains from stage II of the Wangpingxigou deposit have high Co/Ni ratios (mostly > 1) and Au and As contents similar to those of typical epithermal systems. Moreover, sulfides from this deposit have *in-situ* $^{206}Pb/^{204}Pb$ (17.345–17.417), $^{207}Pb/^{204}Pb$ (15.454–15.514), and $^{208}Pb/^{204}Pb$ (38.138–38.364) ratios similar to those of sulfides from the Donggou deposit, indicating that the two deposits were relevant to a common source. The concentrations of many elements (i.e. Pb, Ag, Sn, Zn, Sb, Mn, Au and As) in pyrite decrease gradually from the stage II of the Wangpingxigou deposit to the stage II of the Donggou deposit, consistent with metal zonation typically observed in porphyry related metallogenic systems. Further considering similar ages of the two deposits, we propose that the Wangpingxigou Pb-Zn deposit is likely distal to the Donggou porphyry Mo system.

The range of $\delta^{34}S$ values of pyrites (7.63–8.76‰) from the stage II in the Donggou deposit is similar to those of the ancient strata (Xiong'er Group) (7.31–8.17‰) in the ore district, indicating that the sulfur in ore-forming fluids may be mainly derived from the ancient strata. However, the $\delta^{34}S$ values (9.20–9.70‰) of Stage III sulfides in the Donggou deposit are higher than those of stage II sulfides in the Donggou deposit and stage II sulfides in the Wangpingxigou deposit (7.34–9.29‰). The different sulfur isotopic compositions may be related to varied physicochemical conditions of the ore-forming fluids. Confirmation of a Mo-Pb-Zn metallogenic system in the region provides important clues on further prospecting of Mo and Pb-Zn resources in the southern margin of the North China Craton.

1. Introduction

It is well known that the southern margin of the North China Craton (NCC) is one of the important polymetallic metallogenic provinces in China, which is rich in Mo, Au, Ag, Pb, Zn and W resources (Ye, 2006; Mao et al., 2008; Chen et al., 2009; Mao et al., 2010a; Fig. 1). Many studies have been carried out on these deposits, but mostly focused on the molybdenum and gold deposits. The genesis of spatially associated lead-zinc deposits are not well-known (Chen et al., 2000; Mao et al., 2011b; Li et al., 2012, 2017). Although many vein-type Pb $\pm$ Zn $\pm$ Ag $\pm$ Au deposits in the periphery of porphyry Cu $\pm$ Au $\pm$ Mo deposits were considered as parts of porphyry systems (Sinclair, 2007; Sillitoe, 2010; Mao et al., 2010b, 2011a), it has long been controversial on the genetic relationships between the Pb-Zn and Mo deposits in the southern margin of the NCC (Chen et al., 2004; Cao et al., 2015; Zhang et al., 2016; Li et al., 2017). Some scholars suggested that the peripheral Pb-Zn deposits may represent distal facies of the porphyry system (Ye, 2006; Mao et al., 2008, 2009; Li, 2013; Cao et al., 2015; Li et al., 2017),
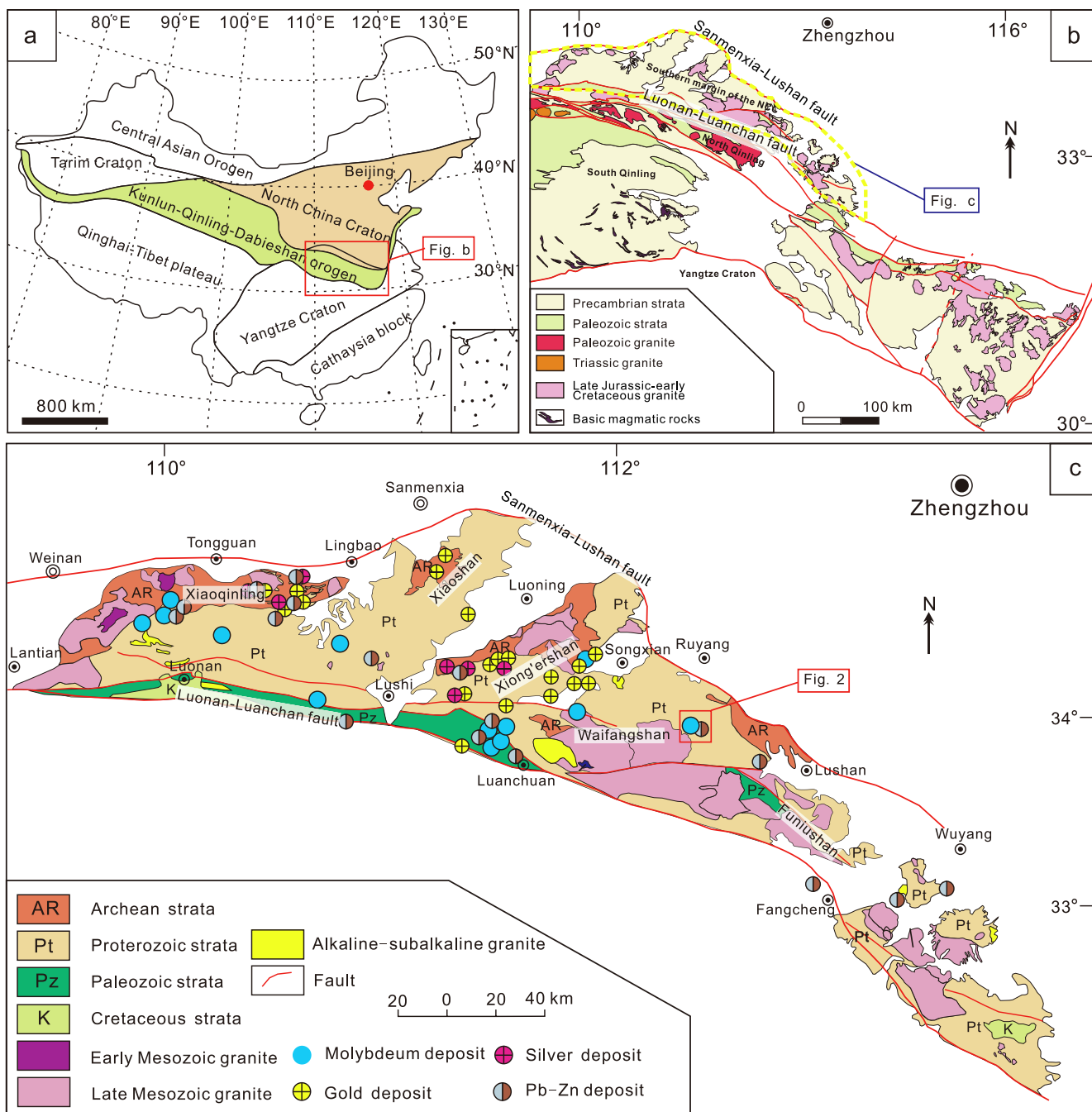
Fig. 1. Distribution of the Mesozoic granitoids and deposits in the southern margin of the North China Craton. (a) Simplified tectonic map of China showing major tectonic phases surrounding the North China Craton and the location of the Qinling Orogenic Belt. (b) Geological map of the Qinling Orogenic Belt (modified from Zhang et al., 1996). (c) Distribution of the Mesozoic granitoids and deposits in the southern margin of the North China Craton.

whereas some researchers suggested that the Ag-Pb-Zn deposits were formed in a continental collision regime and the ore-forming fluid was metamorphic in origin, i.e., without genetic relationship with porphyry system (Chen et al., 2004; Qi et al., 2007; Yao et al., 2008; Zhang et al., 2016). A Mississippi Valley type (MVT) and/or sedimentary exhalative (SEDEX) model is also proposed in a few studies (Yan, 2004; Liu et al., 2007).

    Recent advances in *in-situ* microanalytical techniques permit us to subtly probe the mineral and isotope geochemistry of sulfides, and thus can provide the information on the metal source and the ore-forming process (Barker et al., 2009; Cook et al., 2009; Large et al., 2009; Li et al., 2015, 2017; Li and Zhou, 2018). Pyrite is a major constituent in a wide variety of hydrothermal ore systems, and can contain a series of

trace elements such as Au, Ag, Cu, Pb, Zn, Co, Ni, As, Sb, Se, Te, Tl and Bi (Cook and Chryssoulis, 1990; Reich et al., 2013; Vikentiev et al., 2016), which can provide useful information for understanding the ore-forming processes and physicochemical conditions (Large et al., 2009; Reich et al., 2013; Zheng et al., 2013; Zhang et al., 2014; Keith et al., 2016; Li et al., 2017). Moreover, *in-situ* Pb and S isotopic compositions of sulfides can be employed to identify the source of the ore-forming fluids (Barker et al., 2009; Li et al., 2018; Wu et al., 2018; Zhao et al., 2018a,b).

    In order to delineate the relationship between the porphyry Mo and vein-type Pb-Zn deposits in the peripheral of the granite porphyry, detailed geological and geochemical studies have been carried out on the spatially associated Wangpingxigou vein-type Pb-Zn and Donggou
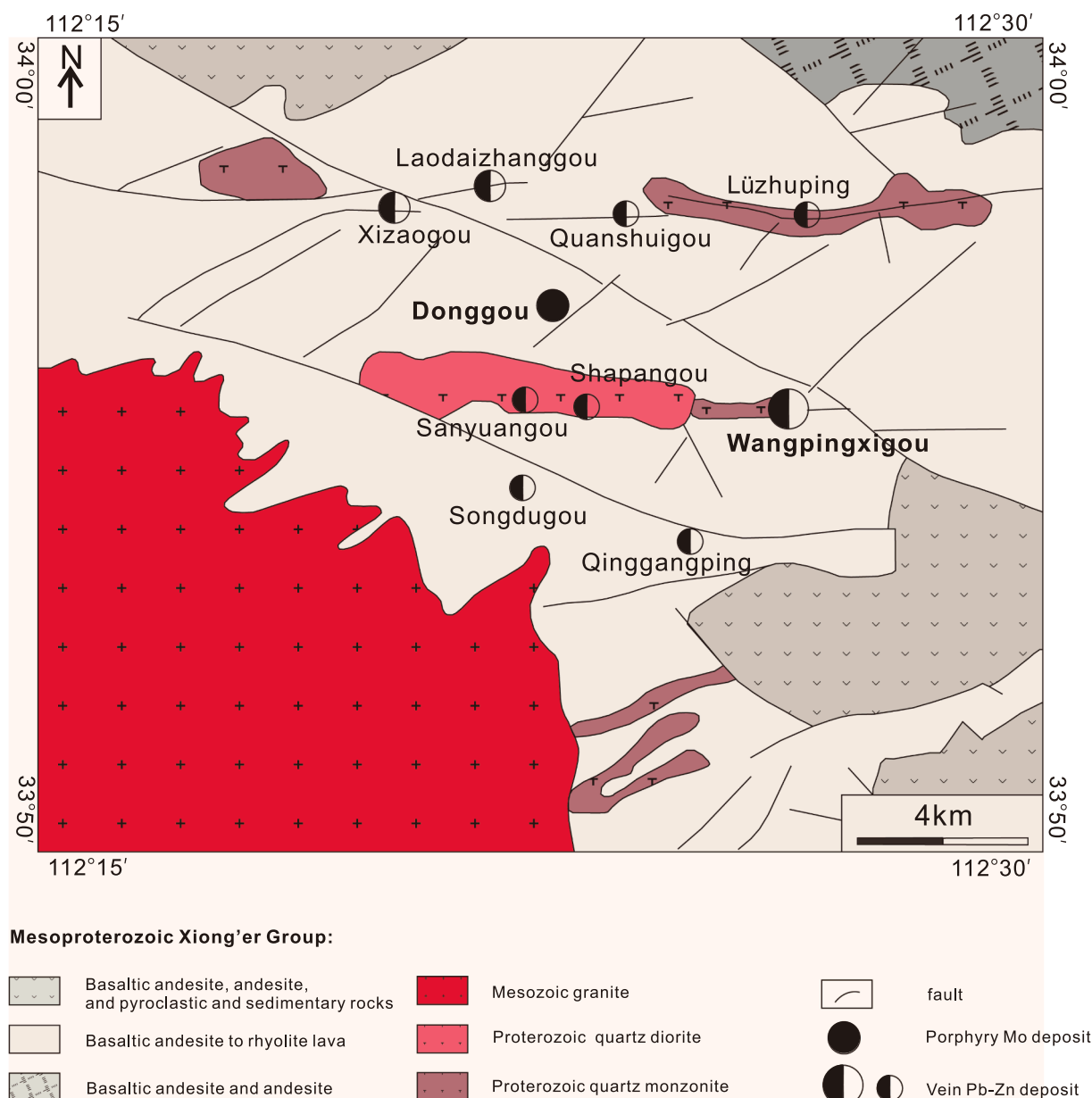
Fig. 2. Simplified geological map of the area around the Donggou porphyry Mo and surrounding Pb-Zn vein deposits (modified from Gao et al. (2014) and Yang et al. (2015)).

porphyry Mo deposits in the southern margin of NCC (Fig. 1). We present new *in-situ* S-Pb isotopic and trace elemental compositions for sulfide minerals, particularly the pyrite. The new dataset, in combination with those in literature, allows us to propose that the Wangping-xigou Pb-Zn deposit is a distal member of the Donggou porphyry Mo deposit in the southern margin of the NCC.

2. Geological background

The East Qinling region is a part of the Qinling orogenic belt which was formed during two collision events in middle Palaeozoic and late Triassic periods, respectively (Meng and Zhang, 1999, 2000; Zhang, 2001; Ratschbacher et al., 2003). The East Qinling orogenic belt consists of four tectonic units, from south to north, including the northern margin of the Yangtze Craton, the South Qinling, the North Qinling and the southern margin of the NCC (Meng and Zhang, 1999, 2000) (Fig. 1b). Since the deposits studied are located in southern margin of the NCC, we only briefly describe the geology of this region here.

The southern margin of the NCC is bounded by the Sanmenxia-Lushan fault to the north and the Luanchuan fault to the south (Fig. 1b). The strata outcropped in the region are the Archean to Paleoproterozoic crystalline basement and overlying Mesoproterozoic to Phanerozoic unmetamorphosed cover sequences. The crystalline basement is composed of metamorphic rocks of the Taihua Group (2.26–2.84 Ga), including amphibolite, felsic gneiss, migmatite, and metamorphosed supracrustal rocks (Kröner et al., 1988; Wan et al., 2006; Xu et al., 2009), which is unconformably overlain by the Mesoproterozoic Xiong'er Group. The Xiong'er Group (1.75–1.78 Ga) is a well-preserved, unmetamorphosed volcanic sequence compositionally dominated by basaltic andesites, andesites and dacites with minor rhyolites, and covers an area of > 60,000 km² (Zhao et al., 2004). The Xiong'er Group is overlain by the Mesoproterozoic littoral clastic rocks and carbonate rocks of the Guandaokou Group and the shallow-sea facies, Neoproterozoic clastic and carbonate rocks of the Luanchuan Group. Paleozoic-Jurassic strata is lacked in the southern margin of the NCC. Since the beginning of the Cretaceous, lacustrine of alluvial sediments began to
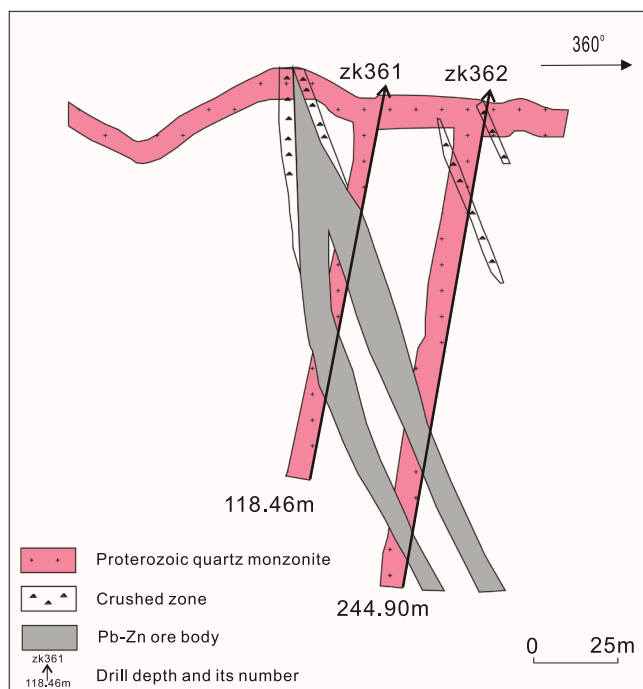
Fig. 3. Cross section along No. 36 exploration line in the Wangpingxigou Pb-Zn deposit (modified from Ma et al. (2006)).

develop in the region.

The Mo mineralization in the sourthern margin of the NCC has four major types, i.e., porphyry, porphyry-skarn, skarn and hydrothermal veins (Mao et al., 2011a,b). Three episodes of Mo mineralization (ca. 233–221 Ma, ca. 148–138 and 131–112 Ma) have been recognized in the East Qinling metallogenic belt during the Mesozoic (Mao et al., 2008; Mao et al., 2011a,b). On the other hand, the Pb-Zn mineralization can be divided into two types according to the occurrences: one occurring at the periphery of the porphyry Mo deposit, another departure from the Mo mineralization or accompanying with gold mineralization (Li, 2013). The timing of the Pb-Zn mineralization is currently not well understood, but available data indicate that the Pb-Zn deposits were likely formed at Early Cretaceous to Middle Cretaceous (144–117 Ma) (Mao et al., 2006; Ye, 2006; Yao et al., 2010; Gao et al., 2011; Li, 2013; Cao et al., 2015; Zhang et al., 2016), broadly synchronous with the Mo mineralization.

3. Deposit geology

In the East Qinling orogenic belt, the Waifangshan district contains abundant porphyry Mo and vein-type Pb-Zn deposits. In this district, vein-type Pb-Zn deposits commonly occur in close proximity of the porphyry Mo deposit, forming a peculiar Mo-Pb-Zn mineralization distribution pattern (Fig. 1c). The Wangpingxigou Pb-Zn deposit is the largest Pb-Zn deposit in this district, about 5 km to the southeast of the Donggou porphyry Mo deposit (Fig. 2). The geological characteristics of the two deposits are described below.

3.1. Wangpingxigou Pb-Zn deposit

The Wangpingxigou Pb-Zn deposit is a large vein-type Pb-Zn deposit, with a proven reserve of 0.6328 Mt lead and zinc metals. The main orebody occurs in a Proterozoic quartz monzonite (Li et al., 2017) (Figs. 3 and 4a), with subordinate orebodies within the Xiong'er Group. Orebodies occur chiefly as lenses and veins in the faults and are broadly parallel to each other. These vein-hosting faults commonly dip 65°–85° to the north, but locally steeply dip to the south. Individual veins are

usually 500–1700 m long and 3–16 m wide. The ore minerals include mainly galena and sphalerite with minor pyrite and chalcopyrite (Fig. 4b–f), and the gangue minerals are dominated by quartz, sericite and calcite (Fig. 4b–f). Rb-Sr isochron of sphalerite from the Wangpingxigou deposit yielded an age of 117 ± 27 Ma (Yao et al., 2010).

Hydrothermal alteration is well developed as linear types around the orebodies, and primarily include sericitization, silicification, chloritization , epidotization and carbonatization (Fig. 4). Yao et al. (2008) recognized three mineralization stages in this deposit: (1) an early, barren stage of quartz – pyrite veins (Stage I) (Fig. 4b); (2) quartz – polymetallic sulfides veins (Stage II) (Fig. 4b–f); (3) post–ore stage of quartz – carbonate veins (Stage III).

3.2. Donggou porphyry Mo deposit

The Donggou porphyry Mo deposit is one of the large Mo deposits in the eastern Qinling metallogenic belt (Jin et al., 2018). This deposit is associated with a granitic porphyry. The granite, with a surface outcrop area of only ~0.01 km^2, is composed of phenocrysts of quartz, plagioclase, perthite, and K-feldspar, with minor amounts of biotite and accessory magnetite, sphene, zircon and rutile. Previous zircon U-Pb dating showed that the formation age of the granite is 118–112 Ma (Ye et al., 2006; Dai et al., 2009; Yang et al., 2013).

The deposit consists of 19 orebodies, 15 of which are located in the outer contact zones of the porphyry and the rest in the altered porphyry (Fig. 5). The orebody is wedge-shaped, with thicknesses ranging from 47 to 254 m. The occurrence of the orebodies is controlled by the contact zones between the porphyry and the Xiong'er Group strata, diping outward from the porphyry stock. The deposit contains a proven reserve of 0.71 Mt Mo metal with an average grade of 0.113% (Li et al., 2007). Molybdenum mineralization is dominated by stockwork veinlets and veins, with minor amounts of sulfide disseminations (pyrite, chalcopyrite, sphalerite and galena) (Fig. 6a–c and e–h). Meanwhile, most magnetite is intergrown with molybdenite (Fig. 6f). The main ore minerals are molybdenite and pyrite, with minor chalcopyrite, sphalerite and galena (Fig. 6). The main gangue minerals consist of quartz, K-feldspar, sericite, chlorite, beryl, fluorite and calcite (Fig. 6). Re-Os isotopic dating on molybdenites from the Donggou deposit yielded ages of 118–114 Ma (Ye et al., 2006; Mao et al., 2008; Li et al., 2017), broadly coeval with the Wangpingxigou Pb-Zn deposit.

Hydrothermal alteration including: (1) silification, mainly associated with quartz ± sulfide veinlets (Fig. 6a-c); (2) potassic alteration, characterized by the replacement of plagioclase by K-feldspar, and the formation of secondary biotite and K-feldspar ± sulfide veinlets (Fig. 6a and b); (3) phyllic alteration, typified by an alteration mineral assemblage of sericite, quartz, and pyrite; (4) propylitic alteration, with pervasive epidote, chlorite and calcite as predominant hydrothermal minerals; (5) fluoritization, represented by disseminated purple fluorite veinlets (Fig. 6g); and (6) carbonation, mainly characterized by calcite veins.

Based on field and microscopic observations on the crosscutting relationships of various veins and paragenetic relationships of hydrothermal minerals, four stages of hydrothermal veins have been identified. Stage I is composed of K-feldspar, quartz, and minor pyrite (Fig. 6a and e). Stage II contains predominantly quartz and molybdenite, with subordinate K-feldspar, pyrite, fluorite and beryl (Fig. 6b, f and g). Stage III is mainly composed of quartz, pyrite, galena, sphalerite, with minor chalcopyrite (Fig. 6c and h). Stage IV is composed of quartz and carbonate.

4. Samples and analytical methods

4.1. In-situ sulfur isotope analyses

Four samples containing pyrite and sphalerite from the Donggou deposit, and two samples containing pyrite and sphalerite from the
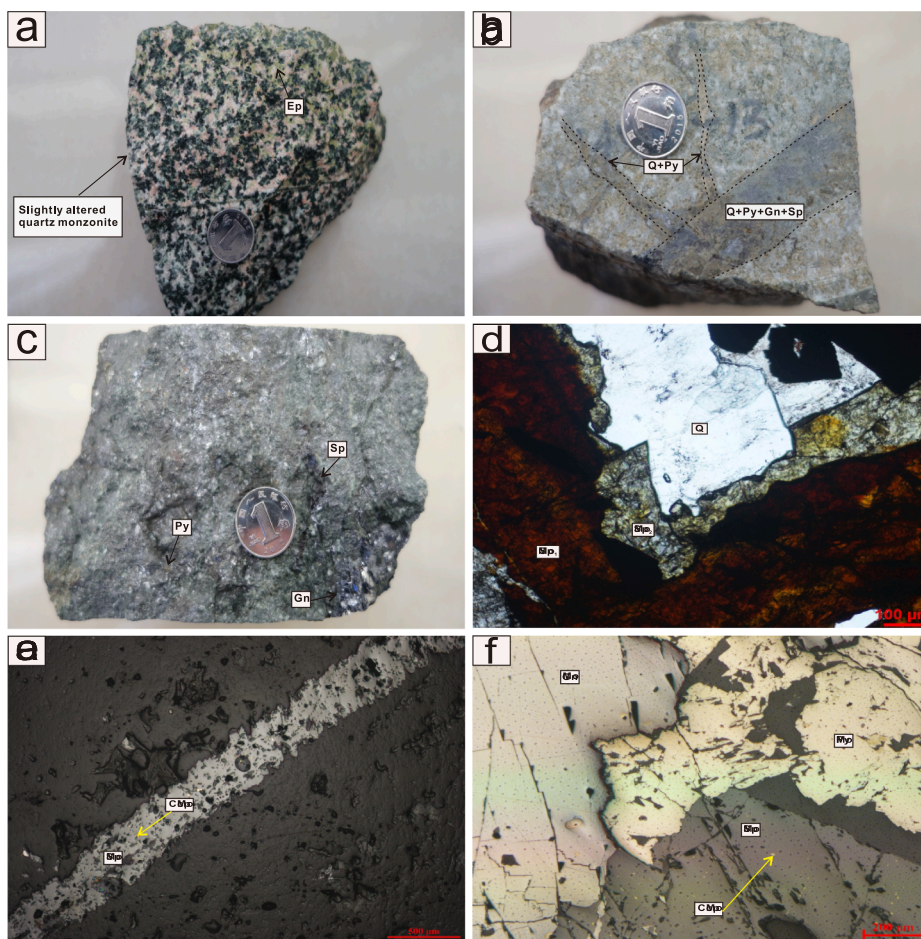
Fig. 4. Photographs and photomicrographs showing ore geology of the wangpingxigou Pb-Zn deposit. (a) slightly altered quartz monzonite; (b) stage I quartz-pyrite veinlet cut by stage II quartz-pyrite-galena-sphalerite veinlet in wall rock; (c) massive ore of sphalerite and galena with fine-grained pyrite. (d) light-colored sphalerite-2 growing in the rim of dark-colored sphalerite-1; (e) stage II sphalerite with chalcopyrite inclusions veinlet in wall rock; (f) stage II quartz-polymetallic veinlet, associated with pyrite, sphalerite and galena in the veinlet. Abbreviations: Ccp-chalcopyrite; Ep-epidote; Gn-galena; Py-pyrite; Q-quartz; Sp-sphalerite.
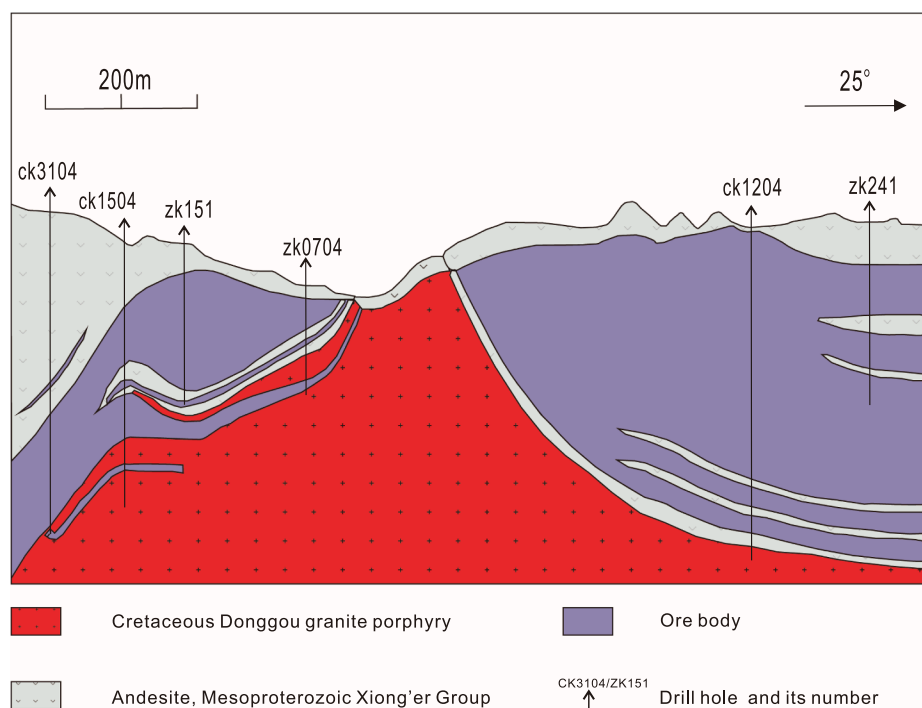

Fig. 5. Cross section along No. 04 exploration line through the Donggou porphyry Mo deposit (modified from Fu et al. (2006)).
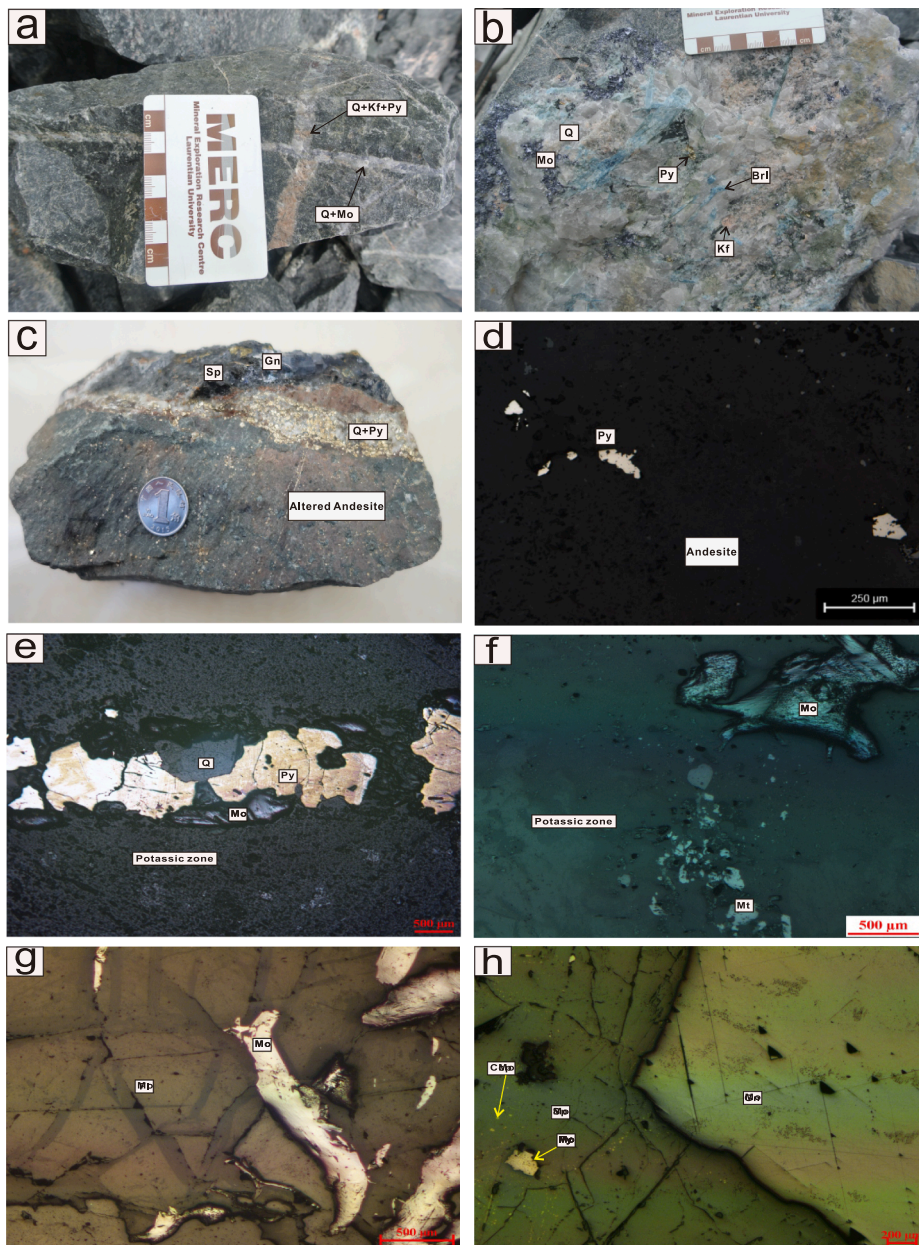
Fig. 6. Photographs and photomicrographs showing ore geology of the Donggou Mo deposit. (a) stage I K-feldspar-quartz-pyrite veinlet cut by stage II quartz-molybdenite veinlet in wall rock; (b) stage II K-feldspar-quartz-beryl-molybdenite-pyrite veinlet; (c) stage III quartz-polymetallic veinlet in altered andesite, associated with pyrite, sphalerite and galena in the veinlet; (d) pyrite in the andesite of the Xiong'er Group; (e) stage I quartz-pyrite veinlet with minor molybdenite cutting the potassic zone; (f) molybdenite intergrown with magnetite in stage II; (g) stage II molybdenite intergrown with fluorite; (h) stage III sphalerite with chalcopyrite and pyrite inclusions intergrown with galena. Abbreviations: Brl-beryl; Fl-fluorite; Kf-k-feldspar; Mt-magnetite; Mo-molybdenite; other abbreviations as in Fig. 4.

Wangpingxigou deposit were selected for *in-situ* sulfur isotope analyses. In addition, two pyrite samples from the Xiong'er Group were analyzed for comparison (Fig. 6d). *In-situ* sulfur isotope analyses were performed using a Nu plasma 1700 multicollector-inductively coupled plasma-mass spectrometer (MC-ICP-MS) equipped with a Resolution M-50 193 nm ArF Excimer laser ablation system at the State Key Laboratory of Continental Dynamics, Northwest University, Xi'an. The analytical procedures are followed those of Bao et al. (2017) and Chen et al. (2017). Samples were ablated in He gas and Ar gas within a two-volume chamber (Laurin Tecnic S-155). During the ablation, data were collected in a static mode (^{32}S, ^{34}S). Single spots of sulfide grains were ablated at a spatial resolution of 37 to 53 um, using a fluence of 3.7 J/cm^2 at 2–4 Hz. The total S signal obtained for sulfides was typically 8–12 V. Under these conditions, a 30 s baseline and a 50 s of ablation were needed to obtain an internal precision of ^{34}S/^{32}S ≤ ± 0.000002 (1 SE). Two pyrite and two sphalerite standards were used for external standard bracketing (Py-4, NBS123) and quality control (PTST-2, PTST-3) of analyses (Chen et al., 2017).

4.2. In-situ Pb isotope analyses

In-situ lead isotopic analyses of different sulfides were conducted on polished sections, using a Nu Plasma™ multi-collector ICPMS with a femtosecond laser ablation system (Fla-MC-ICPMS) at the State Key Laboratory of Continental Dynamics, Northwest University, Xi'an, China. Argon and helium were used as the carrier gases for laser ablation. The Tl aerosol and the sample aerosol was mixed homogeneously in a glass container, and then introduced into the ICP for

atomization and ionization. During the analysis, the Faraday collector L4, L3, L2, L1, AX, H1, H2 were used to collect the ion beam ^{202}Hg, ^{203}Tl, ^{204}Hg + ^{204}Pb, ^{205}Tl, ^{206}Pb, ^{207}Pb, ^{208}Pb, respectively. Thallium was used to monitor and correct for instrumental mass discrimination, and ^{202}Hg was to correct for the isobaric overlap of ^{204}Hg on ^{204}Pb.

The time–resolved analysis (TRA) mode with an integration time of 0.2 s was employed to obtain Pb isotopic ratios, and laser ablation was performed in the line scan ablation mode at a speed of 5 μm/s. Each line scan analysis consisted of background collection for 40 s followed by an additional 50 s of ablation for signal collection and 40 s of wash time to reduce memory effects and to allow the instrument to stabilize after each gas addition. To ensure the stability of ^{208}Pb signal obtained from different samples with disparate Pb concentrations, samples were ablated with laser line scans approximately 120 μm in length and 30–65 μm in width with adjustable laser frequency. NIST 610 was used as a quality control sample, and was analyzed once for every five sample points. Detailed description of the measuring procedures is available in Yuan et al. (2015).

4.3. In-situ LA-ICP-MS trace element analyses of pyrite

Pyrite grains used for LA-ICP-MS spot analyses were observed by a reflected-light microscope to avoid possible contamination of mineral inclusions. Six pyrite samples were selected from stage II and III in the Donggou deposit, and three pyrite samples from the stage II in the Wangpingxigou Pb-Zn deposit for in-situ LA-ICP-MS trace analyses.

The analyses were conducted by an Agilent 7700x quadrupole ICP-MS coupled to an Analyte Excite laser ablation system at Nanjing FocuMS Technology Company Limited. The 193 nm ArF excimer laser, homogenized by a set of beam delivery systems, was focused on sulfide surface with fluence of 4.0 J/cm^2. Ablation protocol employed a spot diameter of 40 um at 7 Hz repetition rate for 40 s (equating to 280 pulses). Helium was applied as a carrier gas to efficiently transport aerosol to ICP-MS. To allow quantification of pyrites, standardization was achieved via external calibration against United States Geological Survey (USGS) synthetic basaltic glass reference material GSE-1G, coupled with ablation yield correction via normalization to 100% total element abundance (Halicz and Günther, 2004), performed on a spot-by-spot basis. To extend the calibration of S, which is not present in GSE-1G, surrogate calibration was applied using S/Fe sensitivity ratios determined by ablation of pure pyrrhotite. The methodology outlined above provides quantitative analysis without prior knowledge and input of internal standard element concentrations for each ablation spot and it is the most appropriate approach to calculate concentrations for spots that sample more than one mineral phases (Gao et al., 2015).

5. Results

5.1. S Isotopic compositions

In-situ S isotopic compositions of samples from the Wangpingxigou and Donggou deposits are summarized in Table 1. Most grains are homogeneous in BSE images and almost contain no mineral inclusions in pyrite and sphalerite grains (Fig. 7). Even if minor grains contain some mineral inclusions, the inclusions were carefully avoided during analyses.

In the Wangpingxigou Pb-Zn deposit, the δ^{34}S values of sulfides range from 7.34 to 9.29‰, with an average value of 8.24‰ (n = 12) (Fig. 8). Among them, the δ^{34}S values range from 7.34 to 8.56‰ for pyrite (n = 6, mean = 7.69‰), and those range from 8.22 to 9.29‰ for sphalerite (n = 6, mean = 8.80‰).

Table 1

In-situ sulfur isotope compositions of pyrite and sphalerite grains from the Xiong'er Group, Donggou porphyry Mo and Wangpingxigou Pb-Zn deposit.

Sample no.	Vein stages	Δ^{34}S$_{V\text{-}CDT}$(‰)	
		Py	Sph
Xiong'er Group			
13DG-22		8.15	
		7.78	
		7.81	
13DG-23		7.57	
		7.31	
		8.17	
Donggou Porphyry Mo deposit			
13DG-08-1-1	II	7.94	
		7.63	
		7.66	
14DG-12		8.73	
		8.55	
		8.76	
15DG-49	III	9.51	9.62
		9.52	9.61
		9.62	9.33
15DG-50		9.20	9.29
		9.70	9.37
		9.46	9.28
Wangpingxigou Zn-Pb deposit			
14WP-11	II	7.50	8.69
		7.66	8.66
		7.74	8.77
14WP-14		8.56	9.29
		7.34	9.15
		7.35	8.22

In the Donggou porphyry Mo deposit, the δ^{34}S values of sulfides range from 7.63 to 9.70‰, with an average value of 9.04‰ (n = 18) (Fig. 8). Specifically, the range of δ^{34}S values is 7.63–9.70‰ for pyrite (n = 12, mean = 8.86‰), and 9.28–9.62‰ for sphalerite (n = 6, mean = 9.42‰).

5.2. Pb isotope compositions

In-situ Pb isotopic compositions of sulfides are listed in Table 2 and plotted in Fig. 9. The Pb isotope values presented here are present-day values, which in most case reflect "initial" isotope values at the time of deposition, because most sulfides (i.e., pyrite, galena, and molybdenite) generally have low U and Th contents (Leng et al., 2015). The various sulfides from the Wangpingxigou deposit have ^{206}Pb/^{204}Pb, ^{207}Pb/^{204}Pb, and ^{208}Pb/^{204}Pb values of 17.345–17.417, 15.454–15.514 and 38.138–38.364, respectively. The sulfides from the Donggou deposit have ^{206}Pb/^{204}Pb, ^{207}Pb/^{204}Pb, and ^{208}Pb/^{204}Pb values of 17.380–17.523, 15.435–15.576 and 38.210–38.507, respectively (Fig. 9).

5.3. Trace elements of pyrite

In-situ LA-ICP-MS trace elemental compositions of pyrite from the Donggou and Wangpingxigou deposits are listed in Appendix A. The average values of trace element contents in pyrite are listed in Table 3. The time-resolved depth profiles for pyrites are relatively smooth (Fig. 10), with no spikes, and this there are almost no interferences of mineral inclusions.

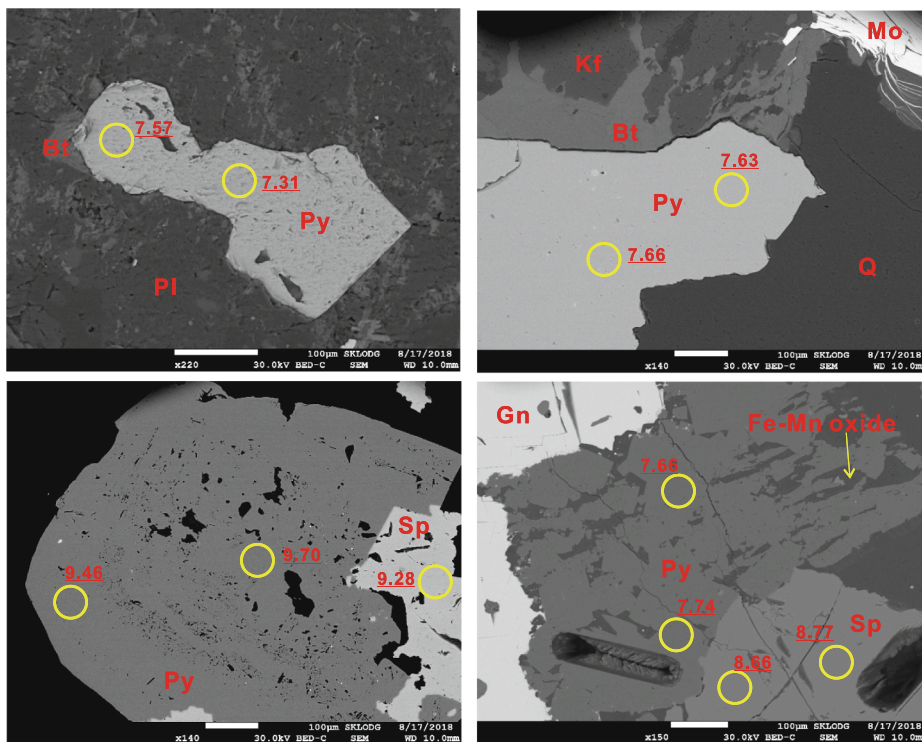Compared to pyrites of the Wangpingxigou Pb-Zn deposit, pyrites

Fig. 7. Representative BSE images showing sulfide grains in the Xiong'er Group, Donggou and Wangpingxigou deposits. (a) subhedral pyrite in close association with biotite and plagioclase in the andesite of the Xiong'er Group; (b) anhedral pyrite intergrown with molybdenite in stage II of the Donggou deposit; (c) subhedral pyrite intergrown with sphalerite in stage II of the Donggou deposit; (d) broken pyrite intergrown with sphalerite and galena in stage II of the Wangpingxigou deposit. Abbreviations: Bt-biotite; Pl-plagioclase; other abbreviations as in Fig. 4 and Fig. 5.
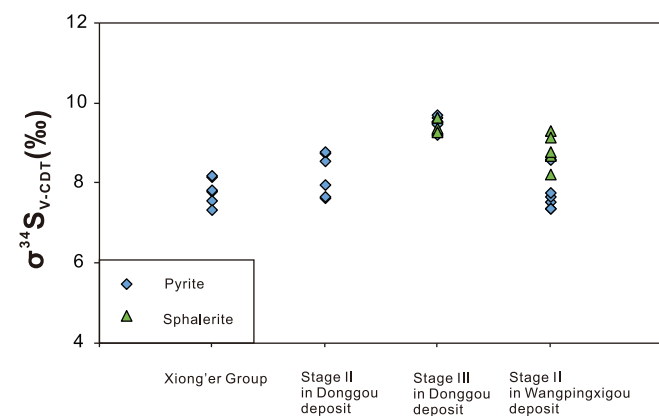

Fig. 8. *In-situ* δ^{34}S values of various sulfides from the Xiong'er Group and different stages of the Donggou and Wangpingxigou deposits.

from the Donggou porphyry Mo deposit are depleted in most trace elements, but contain higher amounts of Co (4.6–3642 ppm), Mo (below detection limit to 76.7 ppm) and Bi (below detection limit to 4.27 ppm) (Figs. 11 and 12a). In contrast, pyrites from the Wangpingxigou have elevated concentrations of Mn (3.70–345 ppm), Zn (42.8–1416 ppm), As (3.44–3524 ppm), Ag (3.36–62.8 ppm), Sn (20.6–3118 ppm), Sb (11.7–180 ppm), Au (0–5.15) and Pb (108–389 ppm) (Figs. 11 and 12b). In addition, pyrites from stage III of the Donggou deposit and the main stage II of the Wangpingxigou deposit have similar Ni (0.15–114 vs. 0.45–314 ppm) contents, with the highest Ni value (5.58–378 ppm) in pyrite from stage II of the Donggou deposit. Moreover, pyrites from the Wangpingxigou and Donggou deposits have similar Co/Ni ratios (< 1–92 vs. < 1–114). As a whole, the

elements (Mo and Bi) increase gradually from the main Pb-Zn mineralization stage of the Wangpingxigou deposit, through the stage III, to the stage II of the Donggou deposit (Fig. 11a), whereas the other elements (Pb, Ag, Sn, Zn, Sb, Mn, Au and As) show a reverse distribution pattern and increase continuously (Fig. 11b–d and Fig. 12b).

6. Discussion

6.1. Wangpingxigou Pb-Zn deposit as a distal member of the Donggou porphyry system

Early Rb-Sr analyses on sphalerite from the Wangpingxigou deposit have yield an age of 117 ± 27 Ma (Yao et al., 2010). Such an age is broadly similar to the molybdenite Re-Os age of the Donggou deposit (118–114 Ma; Ye et al., 2006; Mao et al., 2008; Li et al., 2017). However, although both deposits are spatially closely associated, it is still unclear if they belong to a common magmatic-hydrothermal system. Indeed, the ore-forming fluid for the Wangpingxigou Pb-Zn deposit was interpreted to be magmatic-hydrothermal (Ye, 2006; Mao et al., 2011a,b) or metamorphic origin (Yao et al., 2008).

Pyrite trace elements content can shed light on its origin (Bralia et al., 1979; Deol et al., 2012; Deditius et al., 2014). The Co/Ni ratios in pyrites from the Wangpingxigou deposit are mostly higher than 1 (Fig. 12a), probably indicating a magmatic-hydrothermal origin (Bralia et al., 1979; Deol et al., 2012). Pyrite from the main mineralization stage (stage II) in this deposit has Au and As contents similar to those in the epithermal systems (Fig. 11b). In addition, sulfides from the two deposits have broadly similar ranges of S-Pb isotopic compositions (Figs. 8 and 9), thus indicating that both Pb and S of the two deposit have a common source.

The chemistry of pyrite can also be used to delineate the relationship of the spatially associated Pb-Zn and Mo deposits. Pyrites from the

Table 2

In-situ Pb isotopic compositions of the sulfides from the Donggou porphyry Mo and Wangpingxigou Pb-Zn deposits.

Sample no.	Vein stages	Analyzed mineral	$^{208}Pb/^{204}Pb$	± 1σ	$^{207}Pb/^{204}Pb$	± 1σ	$^{206}Pb/^{204}Pb$	± 1σ	μ
Donggou Porphyry Mo deposit									
13DG-08-1	II	Molybdenite	38.388	0.026	15.488	0.011	17.488	0.012	9.36
			38.371	0.008	15.478	0.003	17.489	0.003	9.34
			38.308	0.030	15.470	0.012	17.438	0.013	9.33
			38.315	0.074	15.463	0.029	17.466	0.034	9.31
		Pyrite	38.283	0.052	15.469	0.021	17.427	0.024	9.33
13DG-08-2	II	Molybdenite	38.283	0.145	15.435	0.058	17.426	0.066	9.26
			38.297	0.081	15.455	0.033	17.439	0.037	9.3
			38.449	0.044	15.514	0.018	17.498	0.020	9.41
			38.506	0.020	15.484	0.008	17.522	0.009	9.35
14DG-12	II	Molybdenite	38.336	0.008	15.478	0.003	17.428	0.003	9.35
			38.341	0.006	15.471	0.002	17.440	0.003	9.33
			38.388	0.008	15.468	0.003	17.471	0.004	9.32
		Pyrite	38.810	0.157	15.505	0.063	18.563	0.082	9.26
			38.343	0.044	15.445	0.018	17.495	0.020	9.27
			38.411	0.012	15.470	0.004	17.472	0.004	9.33
15DG-13-2	II	Molybdenite	39.073	0.093	15.556	0.037	18.574	0.045	9.36
			39.006	0.028	15.548	0.011	18.459	0.016	9.36
			38.914	0.056	15.474	0.017	18.384	0.024	9.22
15DG-49	III	Sphalerite	38.210	0.025	15.448	0.010	17.380	0.011	9.3
			38.257	0.044	15.461	0.018	17.386	0.020	9.32
		Pyrite	38.507	0.071	15.576	0.028	17.523	0.033	9.54
			38.426	0.154	15.510	0.061	17.431	0.071	9.42
			38.286	0.039	15.474	0.016	17.391	0.018	9.35
		Galena	38.333	0.006	15.490	0.002	17.430	0.002	9.38
			38.339	0.011	15.490	0.004	17.426	0.005	9.38
15DG-50	III	Sphalerite	38.312	0.032	15.486	0.013	17.420	0.014	9.37
			38.210	0.031	15.444	0.013	17.381	0.015	9.29
			38.337	0.040	15.499	0.016	17.432	0.018	9.39
		Galena	38.319	0.007	15.486	0.002	17.426	0.002	9.37
			38.327	0.007	15.487	0.002	17.429	0.002	9.37
			38.293	0.005	15.476	0.002	17.401	0.002	9.35
			38.324	0.007	15.488	0.003	17.427	0.003	9.37
		Pyrite	38.300	0.030	15.482	0.012	17.389	0.013	9.37
			38.270	0.012	15.465	0.004	17.398	0.004	9.33
			38.324	0.042	15.489	0.017	17.415	0.018	9.38
Wangpingxigou Pb-Zn deposit									
14WP-11	II	Galena	38.262	0.005	15.493	0.002	17.361	0.002	9.4
			38.269	0.005	15.495	0.002	17.362	0.002	9.4
			38.299	0.006	15.504	0.002	17.382	0.002	9.41
			38.306	0.007	15.506	0.003	17.388	0.003	9.42
		Pyrite	38.198	0.004	15.468	0.001	17.353	0.001	9.34
			38.218	0.004	15.484	0.002	17.365	0.002	9.37
			38.159	0.010	15.462	0.004	17.349	0.005	9.33
			38.138	0.010	15.467	0.004	17.349	0.005	9.34
		Sphalerite	38.193	0.017	15.466	0.007	17.354	0.007	9.34
			38.208	0.024	15.479	0.010	17.373	0.011	9.36
			38.162	0.031	15.454	0.013	17.345	0.014	9.32
14WP-14	II	Sphalerite	38.217	0.015	15.472	0.006	17.364	0.007	9.35
			38.238	0.017	15.483	0.007	17.368	0.008	9.37
			38.151	0.030	15.467	0.012	17.350	0.013	9.34
		Pyrite	38.191	0.045	15.469	0.018	17.352	0.020	9.35
			38.229	0.069	15.489	0.028	17.373	0.032	9.38
		Galena	38.267	0.007	15.493	0.002	17.373	0.002	9.39
			38.269	0.005	15.495	0.002	17.372	0.002	9.4
			38.262	0.008	15.493	0.003	17.371	0.003	9.39
			38.250	0.010	15.490	0.004	17.368	0.003	9.39
14WP-8	II	Galena	38.364	0.004	15.514	0.002	17.417	0.001	9.43
			38.355	0.005	15.511	0.002	17.412	0.002	9.42
			38.351	0.005	15.514	0.002	17.408	0.002	9.43

Wangpingxigou Pb-Zn deposit have higher trace element (except for Mo, Co and Bi) contents than those from the Donggou porphyry Mo deposit (Figs. 11 and 12). The sequential geochemical changes of the pyrites can be the result of water–rock reactions consuming oxygen or desulfidation consuming sulfur during an evolving mineralized sequence (Ward et al., 2017). In addition, pyrites from the stage II in the Donggou deposit and the main metallogenic stage in the Wangpingxigou deposit have Au and As contents similar to porphyry systems and the distal epithermal systems, respectively, whereas those from the stage III in the Donggou deposit have element contents similar to the
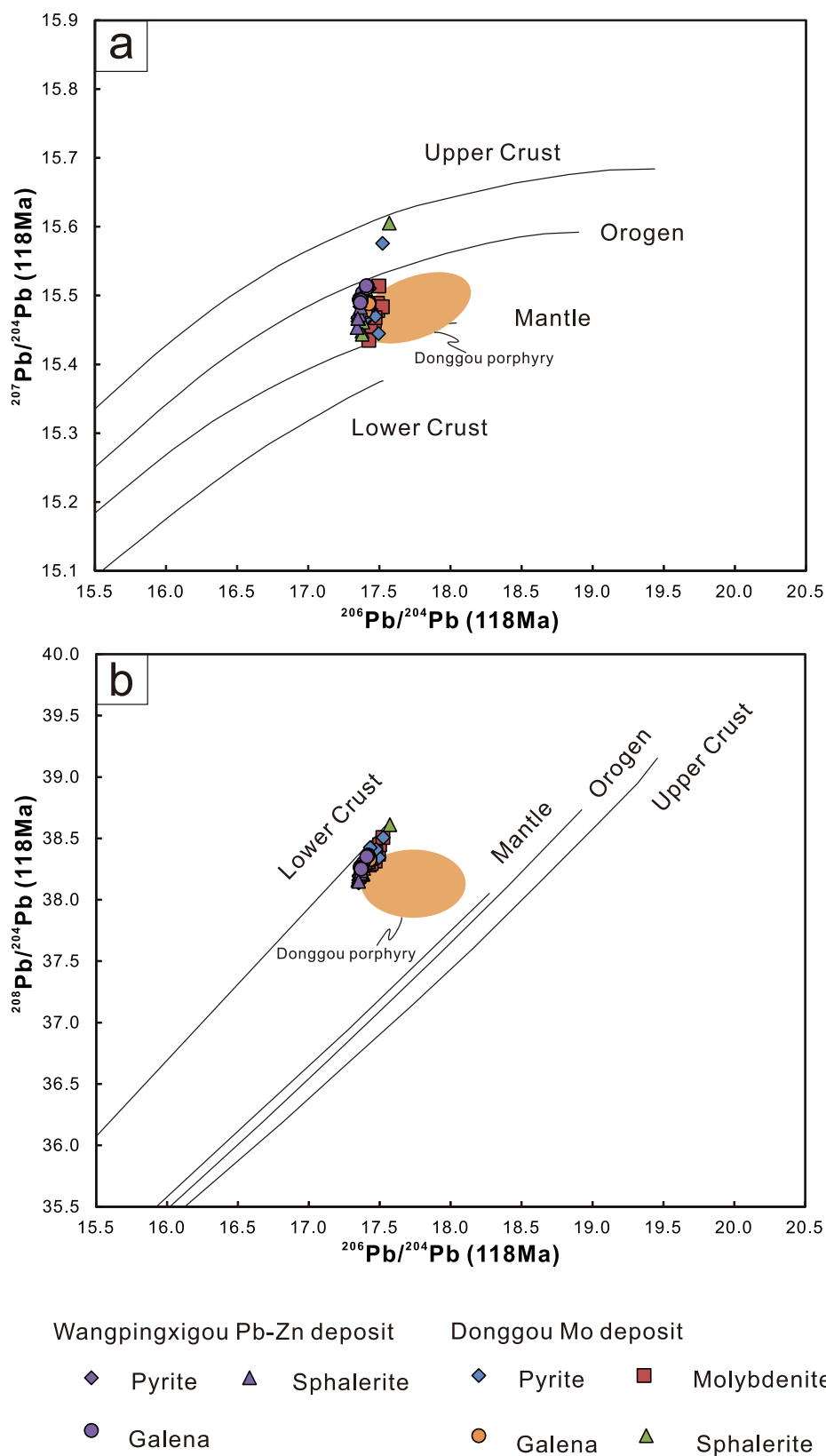
Fig. 9. Plots of $^{207}Pb/^{204}Pb$ vs. $^{206}Pb/^{204}Pb$ and $^{208}Pb/^{204}Pb$ vs. $^{206}Pb/^{204}Pb$ for various sulfides from different vein stages in the Donggou and Wangpingxigou. Data of the Donggou porphyry are from Huang (2009) and Yang et al., (2013). The base diagram is from Zartman and Doe (1981).

Table 3

LA-ICP-MS trace element results (in ppm) of pyrite from the Donggou porphyry Mo and Wangpingxigou Pb-Zn deposits.

	Donggou Mo deposit						Wangpingxigou Pb-Zn deposit		
	Stage II				Stage III		the main metallogenic stage		
	13DG-08–1	15DG-42	14DG-12	15DG-13–1	15DG-49	15DG-50	14WP-11	14WP-1	14WP-14
	ave.(n = 4)	ave.(n = 4)	ave.(n = 2)	ave.(n = 4)	ave.(n = 4)	ave.(n = 4)	ave.(n = 4)	ave.(n = 4)	ave.(n = 4)
S	468,415	464,392	458,368	483,107	439,885	480,415	458,108	493,808	472,188
Fe	530,977	526,623	538,135	516,541	559,674	516,640	538,462	497,986	527,496
Mn	2.17	3.17	5.39	1.43	5.1	13	119	37.5	4.92
Co	161	1243	2181	165	85.6	951	272	46.7	92.0
Ni	202	58.1	142	8.50	11.6	38.1	35.6	95.1	19.6
Cu	7.97	0.13	1.07	0.09	0.28	1.49	102	1498	84.2
Zn	0.36	0.29	1.42	0.39	7.9	2.05	152	1011	603
As	0.88	4.27	37.5	0.63	29.1	233	979	2307	1872
Mo	9.75	1.86	42.9	1.94	1.26	5.4	1.80	0.00	0.30
Ag	0.01	0.02	0.11	0.00	0.06	0.35	35.0	25.6	23.3
Sn	2.01	0.14	6.57	1.91	5.65	11.8	70.6	1208	374
Sb	0.00	0.02	0.06	0.03	0.23	0.53	117	34.5	34.1
Au	0.00	0.00	0.01	0.01	0.00	0.01	0.04	2.40	0.32
Pb	1.37	0.18	2.62	0.01	2.70	17.2	317	286	267
Bi	1.13	1.03	3.24	0.00	0.11	0.78	0.11	0.10	0.21

transitional field between porphyry and epithermal systems (Fig. 12b). Moreover, the positive correlations among elements Bi, Mo, Pb, Ag, Sn, Zn, Sb, Mn, Co and Ni in pyrite from the two deposits (Figs. 10 and 11) are also consistent with an evolution trend for a common fluid. The enrichments of specific trace elements in pyrites from the two deposits are also consistent with metal zonation typically observed in a porphyry-related hydrothermal system, which is commonly characterized by Cu, Mo → Zn, Pb → Ag, Au and As from porphyry ores to distal base-metal veins (Hedenquist and Lowenstern, 1994; Seedorff et al., 2005; Sinclair, 2007; Sillitoe, 2010; Mao et al., 2010b, Mao et al., 2011a).

In summary, both the S-Pb isotopic and trace elemental compositions of sulfides from the Wangpingxigou and Donggou deposits well indicate that they have formed from a common fluid, thus implying that the Wangpingxigou Pb-Zn deposit is likely a distal member of the Donggou porphyry Mo system.

6.2. Source of the ore-forming materials

The primary ores from the mining area are mainly composed of sphalerite, galena, pyrite and molybdenite. The absence of sulfate minerals in the ores indicates that the $\delta^{34}S$ value of the sulfide minerals can generally represent the $\delta^{34}S_{\Sigma S\text{-fluids}}$ value of the hydrothermal fluids (Ohmoto, 1972).

The $\delta^{34}S$ values of sulfides from the Donggou deposit range from 7.63 to 9.70‰, with an average value of 9.04‰ (n = 18), which are significantly higher than most porphyry systems (0 ± 5‰, Ohmoto and Rye, 1979). It is also obviously different from the $\delta^{34}S$ values of sulfides from other Mo deposits at the southern margin of the NCC (such as Jinduicheng, Nannihu, Shangfanggou, Yuchiling and Leimengou, Fig. 13). A few porphyry deposits, such as the Sora and Shakhtama porphyry Mo deposits from Siberia and Diyanqinamu from Inner Mongolia, show similar $\delta^{34}S$ values, with all higher than 5‰ (Fig. 13). Relatively high $\delta^{34}S$ values could either be inherited from the magmatic source, or result from contamination by crustal marine sedimentary facies or evaporates with high $\delta^{34}S$ values (Faure and Brathwaite, 2006). However, the isotopic compositions of Late Mesozoic granites in the southern margin of the NCC are similar, suggesting

a common magmatic source (Gao and Zhao, 2017). Thus, the relatively high $\delta^{34}S$ values are not caused by the magmatic source.

On the other hand, no marine sedimentary facies or evaporites are present in the strata adjacent to the Donggou porphyry Mo and Wangpingxigou Pb-Zn deposits. Even other porphyry Mo deposits that are hosted in the same strata, such as Nannihu and Shangfanggou, the $\delta^{34}S$ values of sulfides are broadly similar to those of porphyry systems (Fig. 13). Therefore, the relatively high $\delta^{34}S$ values might not result from contamination by crustal marine sedimentary facies of evaporates during the evolution of magma.

Considering that the Mesoproterozoic Xiong'er Group is exposed in these two deposits, we must assess the effects of the ancient strata on the contributions of ore-forming materials. The pyrites from the stage II of the Donggou deposit have $\delta^{34}S$ values broadly similar to those from Xiong'er Group (Fig. 8), indicating that the hosting rocks may be the main sulfur source for the Donggou and Wangpingxigou deposits. Moreover, the Pb isotopic ratios of sulfides from the Wangpingxigou and Donggou deposits are broadly consistent with those of the Donggou porphyry (Fig. 9), indicating that the Pb of the two deposits are mainly sourced from the Donggou porphyry. In the $^{207}Pb/^{204}Pb$ vs. $^{206}Pb/^{204}Pb$ and $^{208}Pb/^{204}Pb$ vs. $^{206}Pb/^{204}Pb$ diagrams (Fig. 9; Zartman and Doe, 1981), most of the data are distributed in the area between the orogenic belt (or the lower crust) and the mantle evolution line. Also, these sulfides are characterized by moderate radiogenic Pb isotope values and medium μ values ranging from 9.22 to 9.54, thus further implying that the Pb has a mixing source involving both the crust (average μ at 9.58) and mantle (μ = 8–9; Doe and Zartman, 1979).

It is also important to note that the $\delta^{34}S$ values of pyrite increased from the stage II to the stage III in the Donggou deposit, followed by decrease from the stage II of Donggou deposit to the stage II of Wangpingxigou deposit (Fig. 8). This trend may be related to the variations of the physicochemical conditions (pH, EH, T and the isotopic compostion of sulfur in the fluids) during fluid evolution (Ohmoto, 1972). For example, increases of pH, T and oxidation in fluid are commonly accompanied by a decrease of sulfur isotopic value (Ohmoto, 1972).

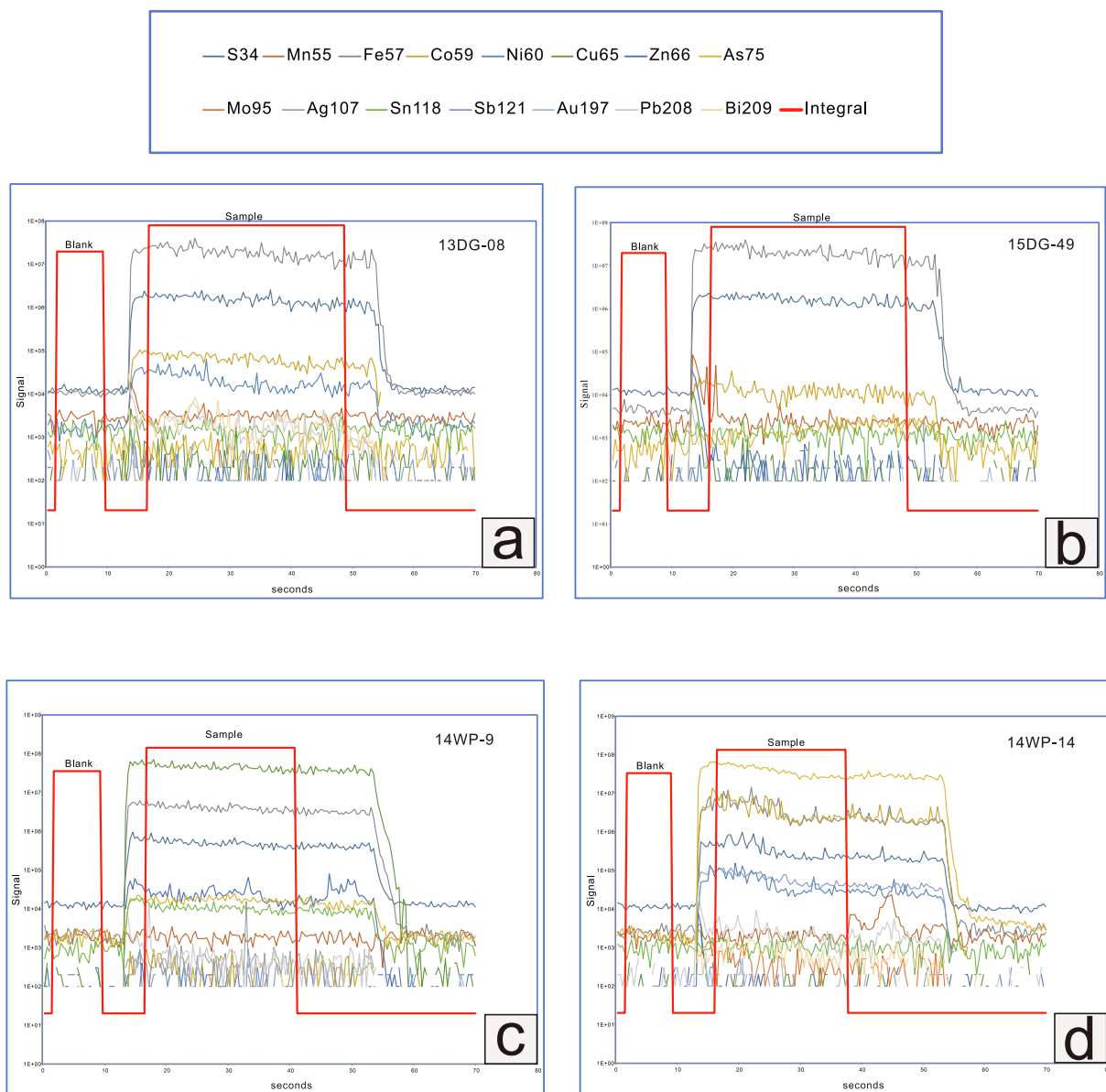The mineralization of stage II in the Donggou deposit is mainly

Fig. 10. Representative time-resolved depth profiles for pyrite analyzed in this study indicating the occurrences of some typical elements. (a) and (b) from stages II and III in the Donggou deposit, (c) and (d) from stage II in the Wangpingxigou deposit.

related to potassic alteration, whereas the stage III is mainly associated to phyllic alteration. This change of alteration is accompanied by decreasing pH (Seedorff and Einaudi, 2004). Meanwhile, magnetite crystallization in stage II of Donggou deposit (Fig. 6f) indicates the increasing oxidation state of the fluid (Sun et al., 2013). Studies of fluid inclusion indicate a decreasing of temperatures and more contributions of meteoritic fluids from stage II to Stage III in the Donggou deposit (Yang et al., 2015). Therefore, the influence of oxidation can be excluded. Moreover, minor change of pH can cause large variation of sulfur isotopic values (Fig. 14). However, such a possibility is not supported by the fact that the variation of sulfur isotopic compositions is limited from the stage II to stage III of Donggou deposit. On the other hand, if the influence of the compositions of the meteoritic fluids is

significant, the trend of variation of sulfur isotopic compositions will be constant from the Donggou to Wangpingxigou deposits, which is not consistent with current data (Fig. 8). In summary, we consider that the temperature may be the major control on the variation of sulfur isotopic compositions from the stage II to the stage III in the Donggou deposit.

Despite the lack of H-O data in Wangpingxigou deposit, the similar temperatures and alteration between the stage III in Donggou deposit and the stage II in Wangpingxigou deposit (Yao et al., 2008; Yang et al., 2015) indicate that both stages have involved similar proportions of meteoric fluids. Hence, the influence of T, pH and compositions of the meteoric fluids on sulfur isotopic compositions can be excluded. This variation may be related to the evolution of sulfur isotope in the ore-forming fluids. Because the heavier sulfur isotope was taken away by
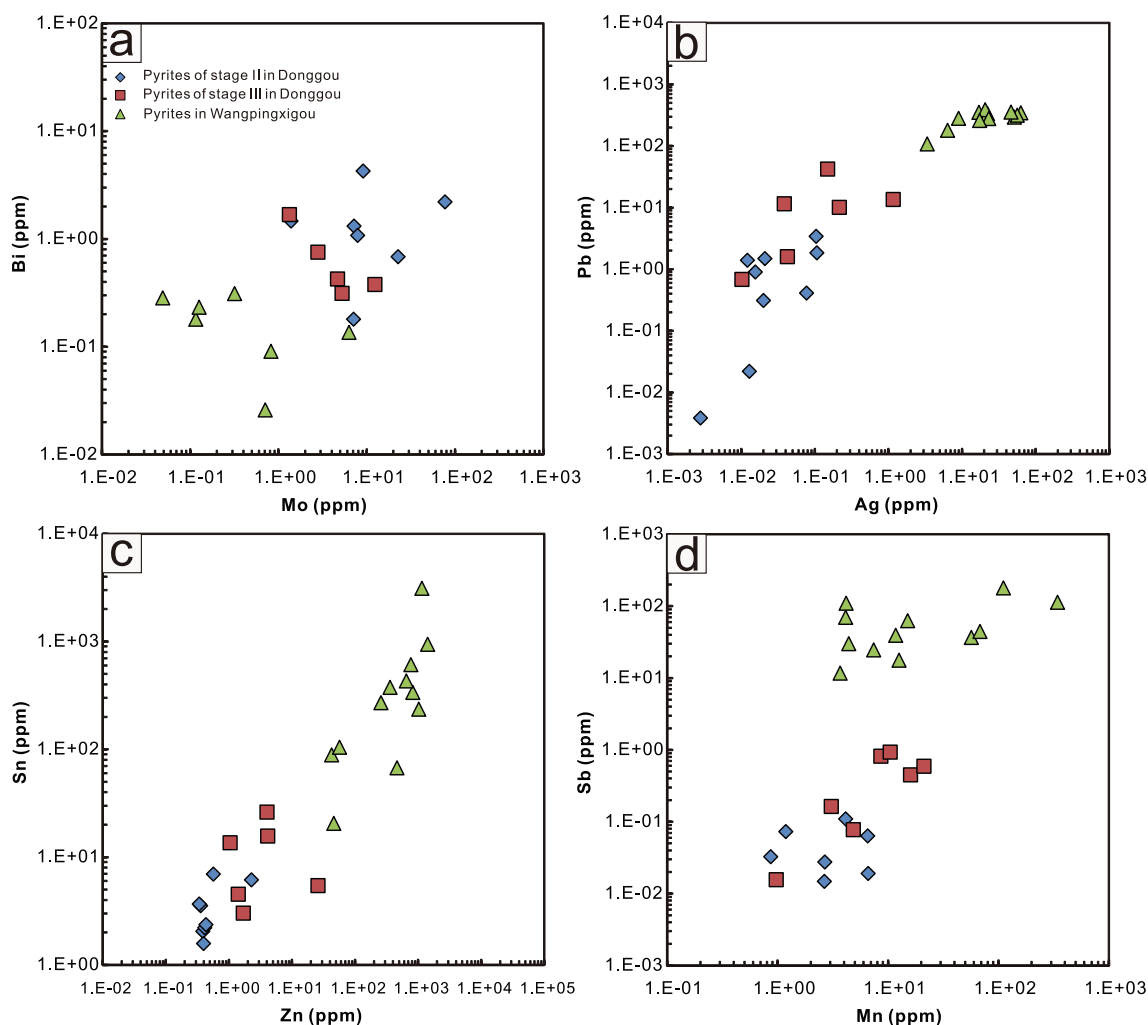
Fig. 11. Binary plot showing the correlation among elements Mo, Bi, Ag, Pb, Zn, Sn, Mn and Sb of pyrite from the Donggou and Wangpingxigou deposits. The contents of trace elements in pyrite are shown in ppm.

the sulfides in the stage II of Donggou deposit. When the sulfides precipitated in the stage II of Wangpingxigou deposit, its sulfur isotopic values may be lighter.

6.3. Implications for mineral exploration

This study illustrates that the Wangpingxigou Pb-Zn deposit is a distal member of the Donggou porphyry Mo deposit system. Similar vein-type Pb-Zn-Ag deposits genetically related to porphyry Mo deposits are also common in the Climax-type or Endako-type Mo metallogenic provinces worldwide (e.g., Stein and Hannah, 1985; Worthington, 2007; Lawley et al., 2010). In the southern margin of the NCC, some magmatic-hydrothermal metallogenic systems have been recognized in several areas. For example, based on the study on the geochronology and isotopic geochemistry, Cao et al. (2015) suggested that porphyry-skarn type Mo-W deposits and peripheral hydrothermal type Pb-Zn-Ag deposits constitute a unified mineralization system in the Luanchuan ore district. Similarly, Zhou (2016) preliminarily established a Mo-Au-Ag-Pb-Zn metallogenic system in the Laomiaogou ore field within the Xiong'er shan area. Our new results, in combination with previous studies on the Waifangshan ore district (Li et al., 2017; Zhao et al., 2018a,b), well suggest that there is a porphyry-related Mo-

Pb-Zn ± Ag metallogenic system in the district.

We further propose that such a Mo-Pb-Zn ± Ag metallogenic system may also exist in the Xiong'er shan area. Mao et al. (2006) identified molybdenite-rich veins in the lower part of the Pb-Zn mineralization of the Shagou deposit, and considered that there would be a porphyry Mo-Pb-Zn metallogenic system in this deposit. Similarly, Li et al. (2016a,b) considered that the Haopinggou Pb-Zn deposit in this area could be genetically related to the proximal Haopinggou porphyry and speculated that the porphyry Mo deposits may occur in the surrounding area of the porphyry. In addition, some Pb-Zn deposits in the Xiaoshan area are discovered recently. Based on the deposit geology, some scholars preliminarily speculated that these Pb-Zn deposits are magmatic-hydrothermal deposits (Li et al., 2016a,b; Zeng et al., 2017). For example, the Zhonghe and Laoliwan Ag-Pb-Zn deposits in the Xiaoshan area are spatially and temporally associated with Zhonghe and Laoliwan granitoids (Li et al., 2016a,b; Zeng et al., 2017). Our study on the genetic relationships between the Wangpingxigou and Donggou deposits provides robust evidence supporting that the Mo-Pb-Zn metallogenic system related to granitic rocks could be widely developed in the southern margin of the NCC. This conclusion provides important implications for prospecting of Mo-Pb-Zn deposits in the region.
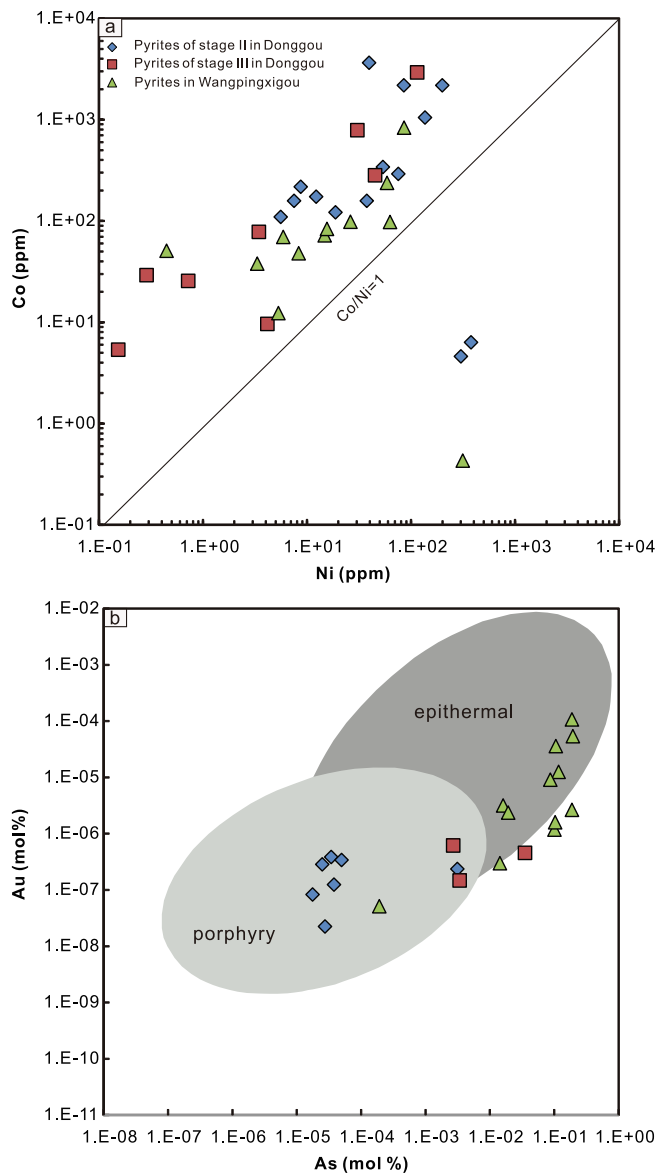
Fig. 12. (a) Correlation between Co and Ni for pyrite from the Donggou and Wangpingxigou deposits; (b) Au-As distribution diagram for pyrite from the Donggou and Wangpingxigou deposits (log-log scale; in mol.%). The boundaries of different deposits are referenced to Deditius et al. (2014).

7. Conclusions

The trace elements of pyrite grains from the Wangpingxigou Pb-Zn deposit to the Donggou porphyry Mo deposit are characterized by an evolution trend. The trend is similar to that displayed by typical a epithermal-porphyry system. The Pb of the Wangpingxigou and Donggou Pb-Zn deposits was derived from a common source involving both the crust and mantle, whereas the S was likely sourced mainly from the Xiong'er Group. The variations of sulfur isotopic compositions in different stages of the two deposits may be related to the variations of the physicochemical conditions of the ore-forming fluids in different stages. Therefore, we consider that the ore-forming fluids for the Pb-Zn and Mo deposits may have been evolved continuously from a common source with the Pb-Zn deposit distal to the porphyry Mo deposit. Such a metallogenic system can be used as a vector for further prospecting of Mo and Pb-Zn resources in the southern margin of the NCC.
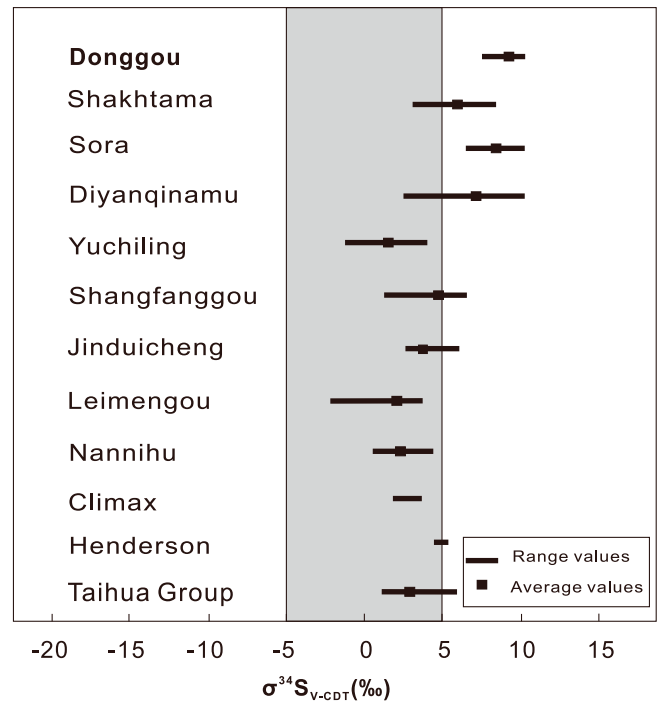

Fig. 13. Comparison of the Donggou Mo deposit with other porphyry Mo deposits. Data for the Donggou deposit are from this study. Data of the Sora and Shakhtama (Sotnikov et al., 2004) porphyry Mo deposits from Siberia, the Diyanqinamu (Leng et al., 2015) porphyry Mo deposit from Central Asian orogenic belt, the Yuchiling (Zhou, 2008), Shangfanggou (Wang et al., 2013 and reference therein), Jinduicheng (Li et al., 2014), Leimengou (Wang et al., 2013 and reference therein) and Nannihu (Wang et al., 2013 and reference therein) porphyry-skarn deposits from the southern margin of the NCC, Henderson and Climax (Stein and Hannah, 1985) porphyry Mo deposits from the North America and related rock units Taihua group (Fan et al., 1994) are also shown for comparison.
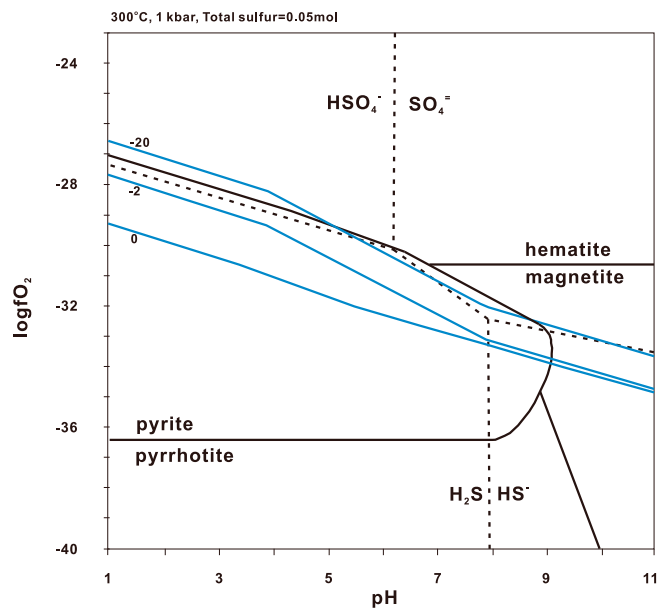

Fig. 14. fO_2 vs. pH plot with sulfur isotopes (blue lines). Modified from Hodkiewicz et al., (2009) after Seward (1973). Conditions set at 300 °C, 1kbar, $\Sigma S = 0.05$ mol, $mNa^+ = 1$, $mK^+ = 0.1$, $MCa^{2+} = 0.01$ and total $\delta^{34}S = 0$‰. (For interpretation of the references to colour in this figure legend, the reader is referred to the web version of this article.)

Appendix A. Supplementary data

Supplementary data to this article can be found online at https://doi.org/10.1016/j.oregeorev.2019.04.005.

References

Bao, Z.A., Chen, L., Zong, C.L., Yuan, H.L., Chen, K.Y., Dai, M.N., 2017. Development of pressed sulfide powder tablets for in situ sulfur and lead isotope measurement using LA-MC-ICP-MS. Int. J. Mass Spectrom. 421, 255–262.

Barker, S.L., Hickey, K.A., Cline, J.S., Dipple, G.M., Kilburn, M.R., Vaughan, J.R., Anthony, A.L., 2009. Uncloaking invisible gold: use of nano SIMS to evaluate gold, trace elements and sulfur isotopes in pyrite from Carlin-type gold deposits. Econ. Geol. 104, 897–904.

Bralia, A., Sabatini, G., Troja, F., 1979. A revaluation of the Co/Ni ratio in pyrite as geochemical tool in ore genesis problems. Mineral. Deposita 14, 353–374.

Cao, H.W., Zhang, S.T., Santosh, M., Zheng, L., Tang, L., Li, D., Zhang, X.H., Zhang, Y.H., 2015. The Luanchuan Mo–W–Pb–Zn–Ag magmatic–hydrothermal system in the East Qinling metallogenic belt, China: constrains on metallogenesis from C–H–O–S–Pb isotope compositions and Rb–Sr isochron ages. J. Asian Earth Sci. 111, 751–780.

Chen, L., Chen, K.Y., Bao, Z.A., Liang, P., Sun, T.T., Yuan, H.L., 2017. Preparation of standards for in situ sulfur isotope measurement in sulfides using femtosecond laser ablation MC-ICP-MS. J. Anal. At. Spectrom. 32, 107–116.

Chen, Y.J., Li, C., Zhang, J., Li, Z., Wang, H.H., 2000. Sr and O isotopic characteristics of porphyries in the Qinling molybdenum deposit belt and their implication to genetic mechanism and type. Sci. China Ser. D Earth Sci. 43, 82–94.

Chen, Y.J., Pirajno, F., Sui, Y.H., 2004. Isotope geochemistry of the Tieluping silver-lead deposit, Henan, China: a case study of orogenic silver-dominated deposits and related tectonic setting. Mineral. Depos. 39, 560–575.

Chen, Y.J., Pirajno, F., Li, N., Guo, D.S., Lai, Y., 2009. Isotope systematics and fluid inclusion studies of the Qiyugou breccia pipe-hosted gold deposit, Qinling Orogen, Henan province, China: implications for ore genesis. Ore Geol. Rev. 35, 245–261.

Cook, N.J., Chryssoulis, S.L., 1990. Concentrations of invisible gold in the common sulfides. Can. Mineral. 28, 1–16.

Cook, N.J., Ciobanu, C.L., Mao, J., 2009. Textural control on gold distribution in As-free pyrite from the Dongping, Huangtuliang and Hougou gold deposits, North China Craton (Hebei Province, China). Chem. Geol. 264, 101–121.

Dai, B.Z., Jiang, S.Y., Wang, X.L., 2009. Petrogenesis of the granitic porphyry related to the giant molybdenum deposit in Donggou, Henan province, China: Constrains from petrogeochemistry, zircon U-Pb chronology and Sr-Nd-Hf isotopes. Acta Petrol. Sin. 2889–2901 (in Chinese with English abstract).

Deditius, A.P., Reich, M., Kesler, S.E., Utsunomiya, S., Chryssoulis, S.L., Walshe, J., Ewing, R.C., 2014. The coupled geochemistry of Au and As in pyrite from hydrothermal ore deposits. Geochim. Cosmochim. Acta 140, 644–670.

Deol, S., Deb, M., Large, R.R., Gilbert, S., 2012. LA-ICPMS and EPMA studies of pyrite, arsenopyrite and loellingite from the Bhukia-Jagpura gold prospect, southern Rajasthan, India: implications for ore genesis and gold remobilization. Chem. Geol. 326, 72–87.

Doe, B.R., Zartman, R.E., 1979. Plumbotectonics, the phanerozoic. Geochem. Hydrotherm. Ore Depos. 2, 22–70.

Fan, H.R., Xue, Y.H., Zhao, R., Wang, Y.L., 1994. Stable isotope geochemistry of rocks and gold deposits in the Xiong'ershan area, Western Henan Province. Contribut. Geol. Miner. Resour. Res. 54–64 (in Chinese with English abstract).

Faure, K., Brathwaite, R.L., 2006. Mineralogical and stable isotope studies of gold–arsenic mineralisation in the Sams Creek peralkaline porphyritic granite, South Island, New Zealand. Mineral. Depos. 40, 802–827.

Fu, Z.G., Song, Y.W., Lu, Y.H., 2006. Ore-controlling geology condition and prospecting information of Donggou Mo deposit in Ruyang, Henan Province. Geol. Prospect. 33–38 (in Chinese with English abstract).

Gao, J.F., Jackson, S.E., Dubé, B., Kontak, D.J., De Souza, S., 2015. Genesis of the Canadian Malartic, Côté Gold, and Musselwhite gold deposits: Insights from LA-ICP-MS element mapping of pyrite. Open File 7852 In: Dubé, B., Mercier-Langevin, P. (Eds.), Targeted Geoscience Initiative 4: Contributions to the Understanding of Precambrian Lode Gold Deposits and Implications for Exploration. Geological Survey of Canada, pp. 157–175.

Gao, J.J., Mao, J.W., Chen, M.H., Ye, H.S., Zhang, J.J., Li, Y.F., 2011. Vein structure analysis and $^{40}Ar/^{39}Ar$ dating of sericite from sub-ore altered rocks in the Tieluping large-size Ag-Pb deposit of western Henan Province. Acta Geol. Sin. 1172–1187 (in Chinese with English abstract).

Gao, X.Y., Zhao, T.P., Bao, Z.W., Yang, A.Y., 2014. Petrogenesis of the early Cretaceous intermediate and felsic intrusions at the southern margin of the North China Craton: Implications for crust–mantle interaction. Lithos 206–207, 65–78.

Gao, X.Y., Zhao, T.P., 2017. Late Mesozoic magmatism and tectonic evolution in the southern margin of the North China Craton. Sci. China Earth Sci. 60, 1–17.

Hedenquist, J.W., Lowenstern, J.B., 1994. The role of magmas in the formation of hydrothermal ore deposits. Nature 370, 519–527.

Halicz, L., Günther, D., 2004. Quantitative analysis of silicates using LA-ICP-MS with liquid calibration. J. Anal. At. Spectrom. 19, 1539–1545.

Huang, F., 2009. A study on the Genesis of the Giant Donggou Porphyry Mo Deposit, Henan Province. A Dissertation for Master's Degree in China University of Geosciences, pp. 1–127 (in Chinese with English abstract).

Hodkiewicz, P.F., Groves, D.I., Davidson, G.J., Weinberg, R.F., Hagemann, S.G., 2009. Influence of structural setting on sulphur isotopes in Archean orogenic gold deposits, Eastern Goldfields Province, Yilgarn, Western Australia. Mineral. Depos. 44, 129–150.

Jin, C., Gao, X.Y., Chen, W.T., Zhao, T.P., 2018. Magmatic-hydrothermal evolution of the Donggou porphyry Mo deposit at the southern margin of the North China Craton: evidence from chemistry of biotite. Ore Geol. Rev. 92, 84–96.

Keith, M., Haase, K.M., Klemd, R., Krumm, S., Strauss, H., 2016. Systematic variations of trace element and sulfur isotope compositions in pyrite with stratigraphic depth in the Skouriotissa volcanic-hosted massive sulfide deposit, Troodos ophiolite. Cyprus. Chem. Geol. 423, 7–18.

Kröner, A., Compston, W., Zhang, G.W., Guo, A.L., Todt, W., 1988. Age and tectonic setting of Late Archean greenstone-gneiss terrain in Henan Province, China, as revealed by single-grain zircon dating. Geology 16, 211–215.

Large, R.R., Danyushevsky, L., Hollit, C., Maslennikov, V., Meffre, S., Gilbert, S., Bull, S., Scott, R., Emsbo, P., Thomas, H., Singh, B., Foster, J., 2009. Gold and trace element zonation in pyrite using a laser imaging technique: implications for the timing of gold in orogenic and carlin-style sediment-hosted deposits. Econ. Geol. 104, 635–668.

Lawley, C.J.M., Richards, J.P., Anderson, R.G., Creaser, R.A., Heaman, L.M., 2010. Geochronology and geochemistry of the MAX porphyry Mo deposit and its relationship to Pb-Zn-Ag mineralization, kootenay Arc, Southeastern British Columbia. Canada Econ. Geol. 105, 1113–1142.

Leng, C.B., Zhang, X.C., Huang, Z.L., Huang, Q.Y., Wang, S.X., Ma, D.Y., Luo, T.Y., Li, C., Li, W.B., 2015. Geology, Re-Os ages, sulfur and lead isotopes of the Diyanqinamu porphyry Mo deposit, Inner Mongolia, NE China. Econ. Geol. 110, 557–574.

Li, H., Ye, H., Wang, X., Yang, L., Wang, X., 2014. Geology and ore fluid geochemistry of the Jinduicheng porphyry molybdenum deposit, East Qinling. China. J. Asian Earth Sci. 79 (Part B), 641–654.

Li, J.W., Bi, S.J., Selby, D., Chen, L., Vasconcelos, P., Thiede, D., Zhou, M.F., Zhao, X.F., Li, Z.K., Qiu, H.N., 2012. Giant Mesozoic gold provinces related to the destruction of the North China Craton. Earth Planet. Sci. Lett. 349–350, 26–37.

Li, M., Huang, C., Fan, G.M., 2016a. Ore fabric characteristics and silver occurrence state of the laoliwan porphyry silver deposit. Mod. Min. 569, 141–144 (in Chinese with English abstract).

Li, N., Chen, Y.J., Zhang, H., Zhao, T.P., Deng, X.H., Wang, Y., Ni, Z.Y., 2007. Molybdenum deposits in East Qinling. Earth Sci. Front. 186–198 (in Chinese with English abstract).

Li, R.C., Chen, H.Y., Xia, X.P., Yang, Q., Danyushevsky, L.V., Lai, C., 2018. Using integrated in-situ sulfide trace element geochemistry and sulfur isotopes to trace ore-forming fluids: example from the Mina Justa IOCG deposit (southern Perú). Ore Geol. Rev. 101, 165–179.

Li, X.C., Zhao, X.F., Zhou, M.F., Chen, W.T., Chu, Z.Y., 2015. Fluid inclusion and isotopic constraints on the origin of the Paleoproterozoic Yinachang Fe-Cu-(REE) deposit, Southwest China. Econ. Geol. 110, 1339–1369.

Li, X.C., Zhou, M.F., 2018. The nature and origin of hydrothermal REE mineralization in the Sin Quyen deposit, Northwestern Vietnam. Econ. Geol. 113, 645–673.

Li, Z.K., 2013. Metallogenesis of the silver-lead-zinc deposits along the southern margin of the North China Craton. A Dissertation for Doctor's Degree in China University of Geosciences, pp. 1–197(in Chinese with English abstract).

Li, Z.K., Li, J.W., Cooke, D.R., Danyushevsky, L., Zhang, L., O'Brien, H., Lahaye, Y., Zhang, W., Xu, H.J., 2016b. Textures, trace elements, and Pb isotopes of sulfides from the Haopinggou vein deposit, southern North China Craton: implications for discrete Au and Ag–Pb–Zn mineralization. Contrib. Mineral. Petrol. 171, 99.

Li, Z.K., Bi, S.J., Li, J.W., Zhang, W., Cooke, D.R., Selby, D., 2017. Distal Pb-Zn-Ag veins associated with the world-class Donggou porphyry Mo deposit, southern North China craton. Ore Geol. Rev. 82, 232–251.

Liu, G.Y., Yan, C.H., Song, Y.W., Duan, S.G., 2007. Characteristics and genesis of Chitudian Lead-Zinc deposits in Luanchuan County. Geol. Surv. Res. 30, 263–270 (in Chinese with English abstract).

Ma, H.Y., Huang, C.Y., Ba, A.M., Li, H.L., Li, F.A., 2006. Metallogenic regularities and prospecting criteria of Pb-Zn-Mo deposits in the south Ruyang area. Geol. Prospect. 17–22 (in Chinese with English abstract).

Mao, J.W., Zheng, R.F., Ye, H.S., Gao, J.J., Chen, W., 2006. $^{40}Ar/^{39}Ar$ dating of fuchsite and sericite from altered rocks close to ore veins in Shagou large-size Ag-Pb-Zn deposit of Xiong'ershan area, western Henan Province, and its significance. Miner. Depos. 359–368 (in Chinese with English abstract).

Mao, J.W., Xie, G.Q., Bierlein, F., Qü, W.J., Du, A.D., Ye, H.S., Pirajno, F., Li, H.M., Guo, B.J., Li, Y.F., Yang, Z.Q., 2008. Tectonic implications from Re–Os dating of Mesozoic molybdenum deposits in the East Qinling-Dabie orogenic belt. Geochim. Cosmochim.

Acta 72, 4607–4626.

Mao, J.W., Ye, H.S., Wang, R.T., Dai, J.Z., Jian, W., Xiang, J.F., Zhou, K., Meng, F., 2009. Mineral deposit model of Mesozoic porphyry Mo and vein-type Pb-Zn-Ag ore deposits in the eastern Qinling, Central China and its implication for prospecting. Geol. Bull. China 28 (1), 72–79 (in Chinese with English abstract).

Mao, J.W., Xie, G.Q., Pirajno, F., Ye, H.S., Wang, Y.B., Li, Y.F., Xiang, J.F., Zhao, H.J., 2010a. Late Jurassic-Early Cretaceous granitoid magmatism in Eastern Qinling, central-eastern China: SHRIMP zircon U-Pb ages and tectonic implications. Aust. J. Earth Sci. 57, 51–78.

Mao, J.W., Zhang, J.D., Guo, C.L., 2010b. Porphyry Cu, epithermal Pb-Zn-Ag, distal hydrothermal Au deposits: a new model of mineral deposit — Taking the Dexing area as an example. J. Earth Sci. Environ. 32 (1), 1–14 (in Chinese with English abstract).

Mao, J.W., Zhang, J.D., Pirajno, F., Ishiyama, D., Su, H.M., Guo, C.L., Chen, Y.C., 2011a. Porphyry Cu-Au-Mo — epithermal Ag-Pb-Zn — distal hydrothermal Au deposits in the Dexing area, Jiangxi province, East China - a linked ore system. Ore Geol. Rev. 43, 203–216.

Mao, J.W., Pirajno, F., Xiang, J.F., Gao, J.J., Ye, H.S., Li, Y.F., Guo, B.J., 2011b. Mesozoic molybdenum deposits in the east Qinling-Dabie orogenic belt: Characteristics and tectonic settings. Ore Geol. Rev. 43, 264–293.

Meng, Q.R., Zhang, G.W., 1999. Timing of collision of the North and South China blocks: Controversy and reconciliation. Geology 27, 123–126.

Meng, Q.R., Zhang, G.W., 2000. Geologic framework and tectonic evolution of the Qinling orogen, central China. Tectonophysics 323, 183–196.

Ohmoto, H., 1972. Systematics of Sulfur and Carbon Isotopes in Hydrothermal Ore Deposits. Econ. Geol. 67, 551–578.

Ohmoto, H., Rye, R.O., 1979. Isotopes of sulfur and carbon. In: Barnes H.L. (ed.), Geochemistry of hydrothermal ore deposits, 2nd ed.: New York Wiley, pp. 509–567.

Qi, J.P., Chen, Y.J., Ni, P., Lai, Y., Ding, J.Y., Song, Y.W., Tang, G.J., 2007. Fluid inclusion constrains on the origin of the Lengshuibeigou Pb-Zn-Ag deposit, Henan province. Acta Petrol. Sin. 2119–2130 (in Chinese with English abstract).

Ratschbacher, L., Hacker, B.R., Calvert, A., Webb, L.E., Grimmer, J.C., McWilliams, M.O., Ireland, T., Dong, S., Hu, J., 2003. Tectonics of the Qinling (Central China): tectonostratigraphy, geochronology, and deformation history. Tectonophysics 366, 1–53.

Reich, M., Deditius, A., Chryssoulis, S., Li, J.-W., Ma, C.-Q., Parada, M.A., Barra, F., Mittermayr, F., 2013. Pyrite as a record of hydrothermal fluid evolution in a porphyry copper system: a SIMS/EMPA trace element study. Geochim. Cosmochim. Acta 104, 42–62.

Seedorff, E., Einaudi, M.T., 2004. Henderson porphyry molybdenum system, Colorado: II. Decoupling of introduction and deposition of metals during geochemical evolution of hydrothermal fluids. Econ. Geol. Bull. Soc. Econ. Geol. 99, 39–72.

Seedorff, E., Dilles, J.H., Proffett, J.M., Einaudi, M.T., Zurcher, L., Stavast, W.J.A., Johnson, D.A., Barton, M.D., 2005. Porphyry deposits: Characteristics and origin of hypogene features. Econ. Geol. 100, 251–298.

Seward, T.M., 1973. Thio complexes of gold and the transport of gold in hydrothermal ore solutions. Geochim. Cosmochim. Acta 37, 379–399.

Sillitoe, R.H., 2010. Porphyry copper systems. Econ. Geol. 105, 3–41.

Sinclair, W., 2007. Porphyry deposits. Mineral deposits of Canada: a synthesis of major deposit-types, district metallogeny, the evolution of geological provinces, and exploration methods: Geological Association of Canada, Mineral Deposits Division. Special Publication, pp. 223–243.

Sotnikov, V., Ponomarchuk, V., Pertseva, A., Berzina, A., Berzina, A., Gimon, V., 2004. Evolution of sulfur isotopes in porphyry Cu-Mo ore-magmatic systems of Siberia and Mongolia. Geologiya i Geofizika 45, 963–974.

Stein, H.J., Hannah, J.L., 1985. Movement and origin of ore fluids in Climax-type systems. Geology 13, 469–474.

Sun, W.D., Liang, H.Y., Ling, M.X., Zhan, M.Z., Ding, X., Zhang, H., Yang, X.Y., Li, Y.L., Ireland, T.R., Wei, Q.R., Fan, W.M., 2013. The link between reduced porphyry copper deposits and oxidized magmas. Geochim. Cosmochim. Acta 103, 263–275.

Vikentiev, I.V., Abramova, V.D., Ivanova, Y.N., Tyukova, E.E., Kovalchuk, E.V., Bortnikov, N.S., 2016. Trace elements in pyrite from the Petropavlovsk gold-porphyry deposit (Polar Urals): results of LA-ICP-MS analysis. Doklady Earth Sci. 470, 976–980.

Wan, Y.S., Wilde, S.A., Liu, D.Y., Yang, C.X., Song, B., Yin, X.Y., 2006. Further evidence for ~1.85 Ga metamorphism in the Central Zone of the North China Craton: SHRIMP U-Pb dating of zircon from metamorphic rocks in the Lushan area, Henan Province. Gondwana Res. 9, 189–197.

Wang, Z.M., Ren, J.G., Zhang, J.F., Ding, G.M., 2013. Geology and sulphur geochemistry of Yechangping molybdenum deposit, western Henan. Miner. Explor. 4, 283–288 (in Chinese with English abstract).

Ward, J., Mavrogenes, J., Murray, A., Holden, P., 2017. Trace element and sulfur isotopic evidence for redox changes during formation of the Wallaby Gold Deposit, Western Australia. Ore Geol. Rev. 82, 31–48.

Worthington, J.E., 2007. Porphyry and other molybdenum deposits of Idaho and Montana. Idaho Geol. Survey Tech. Report 07–3, 22p.

Wu, Y.F., Li, J.W., Evans, K., Koening, A.E., Li, Z.K., O'Brien, H., Lahaye, Y., Rempel, K., Hu, S.Y., Zhang, Z.P., Yu, J.P., 2018. Ore-Forming Processes of the Daqiao Epizonal Orogenic Gold Deposit, West Qinling Orogen, China: constraints from Textures, Trace Elements, and Sulfur Isotopes of Pyrite and Marcasite, and Raman Spectroscopy of Carbonaceous Material. Econ. Geol. 113, 1093–1132.

Xu, X.S., Griffin, W.L., Ma, X., O'Reilly, S.Y., He, Z.Y., Zhang, C.L., 2009. The Taihua group on the southern margin of the North China craton: further insights from U-Pb ages and Hf isotope compositions of zircons. Mineral. Petrol. 97, 43–59.

Yan, C.H., 2004. Study on Inner Structure of Lead-Zinc-Silver Mineralization System in Eastern Qinling. Geological Press, Beijing pp. 1-144 (in Chinese with English abstract).

Yang, L., Chen, F.K., Liu, B.X., Hu, Z.P., Qi, Y., Wu, J.D., He, J.F., Siebel, W., 2013. Geochemistry and Sr–Nd–Pb–Hf isotopic composition of the Donggou Mo-bearing granite porphyry, Qinling orogenic belt, central China. Int. Geol. Rev. 55, 1261–1279.

Yang, Y., Chen, Y., Pirajno, F., Li, N., 2015. Evolution of ore fluids in the Donggou giant porphyry Mo system, East Qinling, China, a new type of porphyry Mo deposit: evidence from fluid inclusion and H-O isotope systematics. Ore Geol. Rev. 65, 148–164.

Yao, J.M., Zhao, T.P., Li, X.H., 2010. Single grain Rb-Sr dating of sphalerite from the Wangpingxigou Pb-Zn deposit in Henan province. Min. Depos. 535–536 (in Chinese with English abstract).

Yao, J.M., Zhao, T.P., Wei, Q.G., Yuan, Z.l., 2008. Fluid inclusions features and genetic type of the Wangpingxigou Pb-Zn deposit, Henan province. Acta Petrol. Sin. 2113–2123 in Chinese with English abstract.

Ye, H.S., 2006. The Mesozoic tectonic evolution and Pb-An-Ag metallogeny in the south margin of North China Craton. A Dissertation for Doctor's Degree in Chinese Academy of Geological Sciences, pp. 1–217 (in Chinese with English abstract).

Ye, H.S., Mao, J.W., Li, Y.F., Guo, B.J., Zhang, C.Q., Liu, W.J., Yan, Q.R., Liu, G.Y., 2006. SHRIMP Zircon U-Pb and Molybdenite Re-Os Dating for the Superlarge Donggou Porphyry Mo Deposit in East Qinling, China, and Its Geological Implication. Acta Geol. Sin. 1078–1088 (in Chinese with English abstract).

Yuan, H.L., Yin, C., Liu, X., Chen, K.Y., Bao, Z.A., Zong, C.L., Dai, M.N., Lai, S.C., Wang, R., Jiang, S.Y., 2015. High precision in-situ Pb isotopic analysis of sulfide minerals by femtosecond laser ablation multi-collector inductively coupled plasma mass spectrometry. Sci. China: Earth Sci. 1285–1293 (in Chinese with English abstract).

Zartman, R.E., Doe, B.R., 1981. Plumbotectonics—the model. Tectonophysics 75, 135–162.

Zeng, W., Chang, Y.Z., Sima, X.Z., Li, C.D., Wang, J.S., Sun, W.Z., Zhang, F., 2017. Zircon U-Pb dating of granite porphyry in Zhonghe silver polymetallic deposit and its geological implication, Xiaoshan area in Henan province. Geol. Survey Res. 40 (2), 81–88 (in Chinese with English abstract).

Zhang, G.W., Guo, A.L., Liu, F.T., Xiao, Q.H., Meng, Q.R., 1996. Three-dimensional architecture and dynamic analysis of the Qinling orogenic belt. Sci. China Ser. D-Earth Sci. 26, 1–6.

Zhang, G.W., 2001. Qinling orogenic belt and continental dynamics. Science Press, Beijing, pp. 1–117 (in Chinese with English abstract).

Zhang, J., Chen, Y., Su, Q., Zhang, X., Xiang, S., Wang, Q., 2016. Geology and genesis of the Xiaguan Ag–Pb–Zn orefield in Qinling orogen, Henan province, China: fluid inclusion and isotope constraints. Ore Geol. Rev. 76, 79–93.

Zhang, J., Deng, J., Chen, H.-Y., Yang, L.Q., Cooke, D., Danyushevsky, L., Gong, Q.J., 2014. LA-ICP-MS trace element analysis of pyrite from the Chang'an gold deposit, Sanjiang region, China: implication for ore-forming process. Gondwana Res. 26, 557–575.

Zhao, H., Sun, W.C., Xie, P., Shen, N.P., Cai, J.L., Luo, M., Li, J., Bao, Z.A., 2018a. Re–Os dating of molybdenite and in-situ Pb isotopes of sulfides from the Lamo Zn–Cu deposit in the Dachang tin-polymetallic ore field, Guangxi. China. Acta Geochim. 37, 384–394.

Zhao, T.P., Zhai, M.G., Xia, B., Li, H.M., Zhang, Y.X., Wan, Y.S., 2004. Zircon U-Pb SHRIMP dating for the volcanic rocks of the Xiong'er Group: Constraints on the initial formation age of the cover of the North China Craton. Chin. Sci. Bull. 49, 2495–2502.

Zhao, T.P., Meng, L., Gao, X.Y., Jin, C., Wu, Q., Bao, Z.W., 2018b. Late Mesozoic felsic magmatism and Mo-Au-Pb-Zn mineralization in the southern margin of the North China Craton: a review. J. Asian Earth Sci. 161, 103–121.

Zheng, Y., Zhang, L., Chen, Y.J., Hollings, P., Chen, H.Y., 2013. Metamorphosed Pb-Zn-(Ag) ores of the Keketale VMS deposit, NW China: Evidence from ore textures, fluid inclusions, geochronology and pyrite compositions. Ore Geol. Rev. 54, 167–180.

Zhou, D., 2016. Metallogenesis of Laomiaogou, Kangshan, Baiu molybdenum-gold-silver-lead-zinc deposits in the Xiong'ershan ore concentration area south margin of the North China Craton. A Dissertation for Doctor's Degree in Chinese Academy od Sciences, Beijing, pp. 1–165(in Chinese with English abstract).

Zhou, K., 2008. Geology, Geochemistry and Metallogenesis of the Yuchiling Porphyry Molybdenum Deposit, Western Henan Province. A Dissertation for Master's Degree in China University of Geosciences, Beijing, pp. 1–78 (in Chinese with English abstract).